

Preservation of Blueschist-facies Minerals along a Shear Zone by Coupled Metasomatism and Fast-flowing CO₂-bearing Fluids

BARBARA I. KLEINE^{1*}, ALASDAIR D. L. SKELTON¹,
BENJAMIN HUET² AND IAIN K. PITCAIRN¹

¹DEPARTMENT OF GEOLOGICAL SCIENCES, STOCKHOLM UNIVERSITY, 106 91 STOCKHOLM, SWEDEN

²DEPARTMENT OF GEODYNAMICS AND SEDIMENTOLOGY, UNIVERSITY OF VIENNA, ALTHANSTRASSE 14, 1090 VIENNA, AUSTRIA

RECEIVED JULY 29, 2013; ACCEPTED JULY 22, 2014
ADVANCE ACCESS PUBLICATION AUGUST 14, 2014

Two types of blue halo (types I and II) composed of blueschist-facies minerals are centered around a brittle, normal shear zone in greenschist-facies rocks on the island of Syros, Aegean Sea, Greece. The shear zone is steeply dipping and cuts a near-horizontal layer of greenschist-facies rocks (albite + epidote + actinolite + chlorite + quartz). Type I and II blue haloes are 0.3 m and c. 1 m wide respectively, and are seen on both sides of the shear zone. The inner type I haloes are composed of nearly pure glaucophane schist and were formed by metasomatic addition of Na₂O and SiO₂, and to a lesser extent of K₂O and large ion lithophile elements (LILE), coupled with loss of CaO, Al₂O₃ and MnO. The outer type II haloes consist of a carbonated blueschist-facies assemblage (glaucophane + calcite + phengite + epidote + garnet + quartz). These experienced only slight metasomatic changes (i.e. addition of K₂O and LILE), which cannot alone explain halo formation. We present petrological, geochemical and thermodynamic evidence that this assemblage was preserved at greenschist-facies conditions because X_{CO₂} was elevated by flow of a CO₂-bearing fluid along the shear zone, which was approximately contemporaneous with greenschist-facies hydration in the surrounding rocks. We further note that the flux of CO₂-bearing fluid along the shear zone was rapid with respect to the fluid flux in the surrounding rocks. Mass-balance calculations reveal that the fluid flux within the shear zone was at least 100–2000 times greater than the fluid flux within the surrounding rocks. Mineral textures show greenschist-facies minerals replacing blueschist minerals in the type II haloes, supporting our interpretation that the blueschist-facies minerals were preserved during greenschist-facies retrogression. A simplified P–T vs X_{CO₂}

pseudosection confirms that preservation of carbonated blueschist can occur at greenschist-facies conditions in the presence of a CO₂-bearing fluid.

KEY WORDS: blueschist preservation; fluid flux calculation; fluid–rock interaction; Si–Na metasomatism; thermodynamic modeling

INTRODUCTION

Investigation of regions where rocks preserve evidence of high-pressure, low-temperature (HP–LT) mineral assemblages provides insights into the processes occurring within subduction zones. However, HP–LT rocks are commonly intensely overprinted at lower pressure (LP) conditions such as in the greenschist or amphibolite facies, which tends to erase the record of former subduction processes (Ernst, 2006). Various mechanisms have been proposed to explain regional and localized preservation of blueschist-facies mineral assemblages at greenschist-facies conditions. Regional-scale preservation could be caused by rapid exhumation (e.g. Avigad, 1993) and/or the absence of retrograde fluids (e.g. Matthews & Schliestedt, 1984; Parra *et al.*, 2002). Localized mechanisms for preservation of HP–LT mineral assemblages rely on metasomatic addition or removal of components (e.g. Beinlich *et al.*, 2010), low permeability (e.g. Bröcker, 1990; Barrientos & Selverstone, 1993), differences in bulk-rock composition

* Corresponding author. Telephone: +46 (0)8 674 77 28. Fax: +46 (0) 8 674 78 97. E-mail: barbara.kleine@geo.su.se

(e.g. Baziotis *et al.*, 2008; Brovarone *et al.*, 2011) or reduced fluid pressure adjacent to impermeable rock layers (e.g. Breeding *et al.*, 2003).

Limited fluid availability and a lack of late deformation appear to be critical factors for preservation of blueschist-facies rocks. However, on the island of Syros (Cyclades, Greece), we observe blueschist preservation at retrograde greenschist-facies conditions along the margins of a heavily carbonated, brittle, normal shear zone. We show that this spatial association arises because the blueschist-facies minerals were preserved by fast-flowing CO₂-bearing fluids along this shear zone, and we attempt to quantify the fluid fluxes that were involved.

Considerable advances have been made towards quantifying time-integrated and time-averaged metamorphic fluid fluxes from the propagation and broadening of reaction and isotope fronts during regional metamorphism (e.g. Bickle & Baker, 1990; Skelton *et al.*, 1995; Skelton, 2011). For example, Skelton (2011) calculated a time-averaged fluid flux rate of $10^{-10.2} \pm 0.4 \text{ m}^3 \text{ m}^{-2} \text{ s}^{-1}$ for regional greenschist-facies metamorphism in the SW Scottish Highlands. Numerous studies have shown that fluid fluxes are even higher within shear zones, where fluids are channeled [see review by Ague (2003a) and references therein]. If these focused fluxes are large enough, they can have a significant impact on mass transfer and the thermal and mechanical structure of the crust (Drury, 1974; Beach & Tarney, 1978; Bickle & McKenzie, 1987; Brady, 1988; Ague, 2003a). Fluid flow along shear zones plays a major role in the crustal fluid-flow budget (Fyfe *et al.*, 1978) and also in localizing mesothermal gold deposits (Mikuchi & Ridley, 1993; Robert *et al.*, 1995). Furthermore, fluid flow might have influenced Earth's climate. CO₂ degassing from orogenic belts has been estimated to be of the order of $>10^{18}$ moles CO₂ Ma⁻¹ (from Kerrick & Caldeira, 1998; Wallmann, 2001a, 2001b), but whether this release occurs slowly at a constant rate or as a series of rapid pulses is unknown. To answer these questions it is essential to know fluid flux rates along faults and shear zones. This was first attempted by Dipple & Ferry (1992), who calculated an average flow rate of 0.0035–0.35 m a⁻¹ within shear zones.

Here, we use a simple mass-balance approach to calculate the fluid flux within a shear zone that would be required to cause the observed preservation of blueschist-facies minerals.

GEOLOGICAL SETTING

Regional setting

Syros forms part of the Cyclades archipelago in the Aegean Sea (Fig. 1a). The island is situated within the Attic–Cycladic metamorphic core complex belt (Aubouin & Dercourt, 1965; Dürr *et al.*, 1978; Jacobshagen *et al.*, 1978; Jolivet & Brun, 2010). The area is now located in the

back-arc of the active Hellenic subduction zone. Detailed descriptions of the tectono-metamorphic evolution of the Cyclades can be found in recent reviews (e.g. Jolivet & Brun, 2010; Ring *et al.*, 2010; Jolivet *et al.*, 2013).

The Attic–Cycladic metamorphic core complex belt consists of two major structural units. The upper unit consists of unmetamorphosed Permian to Mesozoic sedimentary rocks, ophiolites, greenschist-facies rocks of Cretaceous to Tertiary age, and medium-*P*–high-*T* rocks and granitoids of Late Cretaceous age (Reinecke *et al.*, 1982; Patzak *et al.*, 1994; Bröcker & Franz, 1998; Zeffren *et al.*, 2005). The lower unit consists from bottom to top of pre-Alpine crystalline basement and a sequence of metamorphosed volcano-sedimentary rocks that are also known as the Cycladic Blueschist Unit (CBU; Dürr *et al.*, 1978; Okrusch & Bröcker, 1990). The two major units are separated by low-angle normal faults (Avigad *et al.*, 1997; Jolivet *et al.*, 2003).

Blueschist-facies to lower eclogite-facies metamorphism of the subducted sedimentary and magmatic rocks occurred in the Eocene from ~53 Ma to 30 Ma (Ring & Layer, 2003; Tomaschek *et al.*, 2003; Putlitz *et al.*, 2005; Ring *et al.*, 2007) at pressures of 1.2–2.0 GPa and temperatures of 450–550°C (Matthews & Schliestedt, 1984; Schliestedt, 1986; Dixon & Ridley, 1987; Avigad & Garfunkel, 1989, 1991; Okrusch & Bröcker, 1990; Bröcker *et al.*, 1993; Trotet *et al.*, 2001a, 2001b; Rosenbaum *et al.*, 2002; Keiter *et al.*, 2004; Putlitz *et al.*, 2005). Retrograde metamorphism from blueschist-facies to greenschist-facies conditions, which is typically localized along larger shear zones (e.g. Ring *et al.*, 2010), occurred over a long period of time from the Oligocene into the Miocene (Altherr *et al.*, 1982; Wijbrans *et al.*, 1990; Bröcker *et al.*, 1993; Ring & Layer, 2003), probably at 0.8–1.0 GPa and 400–500°C (e.g. Trotet *et al.*, 2001a; Schumacher *et al.*, 2008a).

Geology of Syros

Most rocks on Syros belong to the CBU (Fig. 1b). On Syros the CBU can be subdivided into (1) a volcano-sedimentary sequence containing marbles, carbonate-bearing and carbonate-free metapelites, metabasic rocks, cherts and quartzites and (2) a structurally higher meta-ophiolitic mélange composed of eclogites, glaucophanites, meta-gabbros, ultrabasic rocks, felsic gneisses and jadeitites (Dixon & Ridley, 1987; Bröcker & Enders, 2001). In the southeastern part of Syros a third unit, the Vari gneiss, has been recognized. This unit is of middle to late Cretaceous age (Maluski *et al.*, 1987; Tomaschek *et al.*, 2000). The tectonic stratigraphy of this unit is debated. It has been interpreted as the structurally uppermost unit on Syros (Maluski *et al.*, 1987; Ring *et al.*, 2003; Keiter *et al.*, 2011; Soukis & Stöckli, 2013) or as part of the Variscan basement that underlies the CBU (Philippon *et al.*, 2011). With the exception of the Vari gneiss, the rocks on Syros contain high-*P* mineral assemblages that record metamorphism at

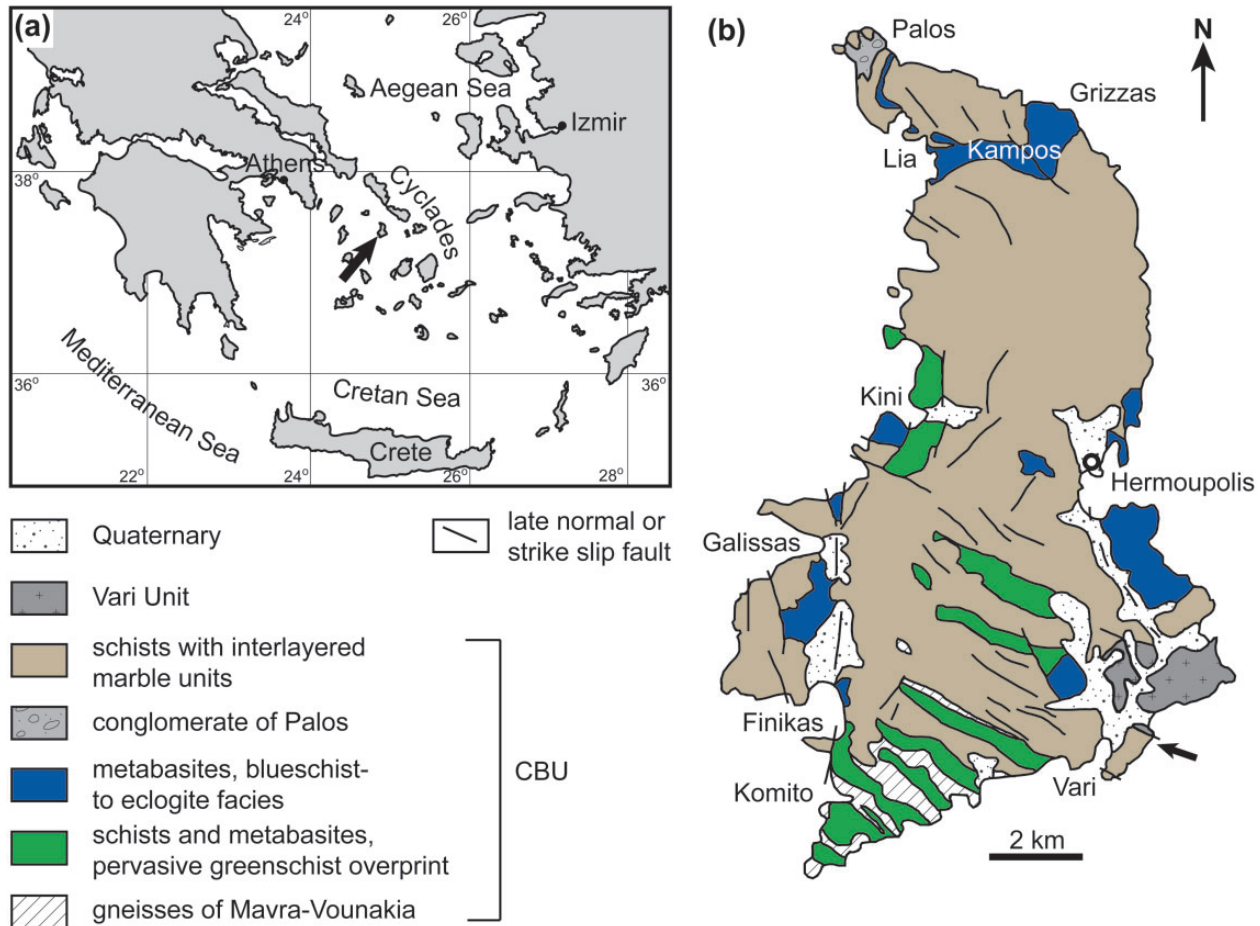


Fig. 1. (a) Location of the Cyclades archipelago. (b) Simplified geological map of Syros [modified after Keiter *et al.* (2011)]. The arrow indicates the study area.

pressures exceeding 15 GPa and temperatures around 500°C (Dixon & Ridley, 1987; Okrusch & Bröcker, 1990).

The P – T evolution of the CBU on Syros remains controversial. Some researchers favor a single unit with a single P – T evolution with peak conditions around 15 GPa and 500°C (Schumacher *et al.*, 2008a, and references therein), whereas Trotet *et al.* (2001a, 2001b) described three metamorphic sub-units separated by normal shear zones, each with peak metamorphism at 1.9 GPa and 525°C, but with different retrograde P – T paths. Peak conditions in the eclogite facies have been dated at 52 Ma based on application of the Lu–Hf method to garnet (Lagos *et al.*, 2007). This result is broadly consistent with age determinations based on U–Pb dating of zircons (Tomaschek *et al.*, 2003) and $^{40}\text{Ar}/^{39}\text{Ar}$ dating of white micas (Maluski *et al.*, 1987; Tomaschek *et al.*, 2003; Putlitz *et al.*, 2005). Greenschist-facies retrogression on Syros is thought to have occurred in Miocene times (e.g. Altherr *et al.*, 1979; Wijbrans *et al.*, 1990; Avigad, 1993; Bröcker *et al.*, 1993, 2004; Trotet *et al.*, 2001a).

Metamorphic fluid flow

Evidence of prograde, retrograde and post-metamorphic fluid flow events has been described in rocks from the Cyclades archipelago. The flow of fluids released during prograde HP–LT metamorphism of subducting oceanic crust is thought to have been strongly channeled, rather than pervasive, resulting in spatially variable fluid fluxes (e.g. Philippot & Selverstone, 1991; Selverstone *et al.*, 1992; Bröcker *et al.*, 1993; Getty & Selverstone, 1994; Barnicoat & Cartwright, 1995; Ganor *et al.*, 1996; Ague, 2000, 2007; Putlitz *et al.*, 2000; Breeding *et al.*, 2003; Ague & Nicolescu, 2014). Prograde metamorphic fluids preferentially leached large ion lithophile elements (LILE), U and Pb as they passed through subducting metasedimentary rocks (Breeding *et al.*, 2004). Retrogression from blueschist to greenschist facies was at least partly facilitated by metamorphic fluid flow at pressures ranging from 0.9 to 0.4 GPa and temperatures ranging from 500 to 350°C (e.g. Schliestedt & Matthews, 1987; Avigad *et al.*, 1992; Bröcker *et al.*, 1993; Parra *et al.*, 2002; Schumacher *et al.*,

2008a). This fluid was ^{18}O -enriched and buffered by exchange with marbles (Schliestedt & Matthews, 1987). Both prograde and retrograde metamorphic fluids on Syros are thought to have been hydrous ($X_{\text{CO}_2} \sim 0.01$), based on mineral equilibria (Schumacher *et al.*, 2008b), and variably saline, based on fluid inclusion studies (Barr, 1990). Swarms of post-metamorphic carbonate and quartz veins cross-cut variably well-preserved and retrograded HP–LT metamorphic rocks on Sifnos, Tinos and Kythnos (Ganor *et al.*, 1994) and were also observed on Syros in our study. The veins studied by Ganor *et al.* (1994) are characterized by low $\delta^{13}\text{C}$ values (ranging from -12% to -8%), which they attributed to oxidation of organic carbon or circulation of surface water through extensional fractures generated during late-stage exhumation. This second explanation is favored by $\delta^{18}\text{O}$ analyses of quartz–calcite veins forming close to the brittle–ductile transition (Famin *et al.*, 2004).

LOCALITY DESCRIPTION

Our study focuses on a locality on Fabrika Beach, which is located on the SE coast of Syros close to the village of Vari ($37^{\circ}23'19.70''\text{N}$, $24^{\circ}57'11.65''\text{E}$).

Overview

The rocks observed on Fabrika Beach belong to the CBU (Fig. 2; Trotet *et al.*, 2001a, 2001b; Keiter *et al.*, 2011). Four main lithologies can be recognized: (1) a layered metavolcanic sequence containing metabasites (with eclogite, blueschist and greenschist mineral assemblages); (2) sequences of garnet–mica quartzites (containing HP–LT mineral assemblages); (3) an impure marble sequence containing HP–LT metabasic lenses; (4) a massive marble layer. Along the coastline, the foliation of the metavolcanic sequence dips gently towards the NW (average foliation 253/31) or to the NE (average foliation 308/31). The stretching lineation strikes approximately east–west. Whether these variations in orientation are related to early ductile deformation or late brittle–ductile deformation is not clear.

Outcrop description

The locality that is the focus of our study lies within the metavolcanic sequence. Here, spectacular relationships can be observed between deformation and fluid flow, as well as clear kinematic indicators (Fig. 3).

The outcrop centres on a brittle to ductile, high-angle, normal shear zone that dips steeply to the NE with a sense-of-shear top-to-the-NE. This is clearly displayed by normal drag of the foliation, which otherwise dips shallowly to the NE. Greenschist-facies metabasites in the footwall of the shear zone are juxtaposed against garnet–mica psammites in its hanging wall. The greenschist-facies metabasites contain chlorite, epidote, actinolite and albite. The shear zone is filled by a breccia, with clasts from both

footwall and hanging wall cemented together by a quartz–carbonate matrix.

Where the shear zone is bordered by greenschist-facies metabasites, we observe two types of blue halo (Fig. 3b and c). Immediately adjacent to the shear zone (within *c.* 20 cm), there is a blue halo composed of glaucophane schist, which we define as a ‘type I blue halo’. This rock contains glaucophane and minor amounts of phengite. Further from the shear zone (from *c.* 20 cm to *c.* 1 m), a blue halo composed of glaucophane, phengite, calcite, epidote and garnet occurs. We define this as a ‘type II blue halo’.

In this study, we explore the origin of the type I and II blue haloes. We present petrological and geochemical evidence that type I blue haloes are of largely metasomatic origin, whereas type II blue haloes are composed of blueschist-facies minerals that have been preserved because of the fast flow of a CO_2 -bearing hydrous fluid along the shear zone.

SAMPLING

Two profiles have been sampled in the footwall and hanging wall perpendicular to the shear zone. Profiles 1 and 2 extend from the sharp boundary between the carbonate–quartz material that fills the normal shear zone and the host-rock (Fig. 3a and b). The profiles cross both types of blue halo and terminate within the greenschist-facies rocks. Samples for petrographic study, electron microprobe and X-ray fluorescence analysis were taken every 10–20 cm along the profiles. Additional samples were taken of vein material within the shear zone and from representative metabasic blueschist-facies and greenschist-facies rocks far from the shear zone.

ANALYTICAL METHODS

Mineral modes were estimated by point counting of 1000 evenly spaced points in eight thin sections from each of profiles 1 and 2, and of representative blueschist- and greenschist-facies rocks far from the shear zone, to provide a quantitative basis for determining possible mineral reactions. Point counting was done with a Leica petrographic microscope equipped with an automated stage driven by PetroLite (v. 2.37) software. Uncertainties were calculated following the approach of Van der Plas & Tobi (1965). Point count data were used to assess if colour changes (from blue to green) along the profiles could be related to modal variations.

Major element analyses were used to assess the relationship of bulk chemical and mineralogical variation along the profiles and were done using a Rigaku ZSX Primus II sequential X-ray fluorescence (XRF) spectrometer at the Department of Geological Sciences at Stockholm University. These data were used to assess the extent to which

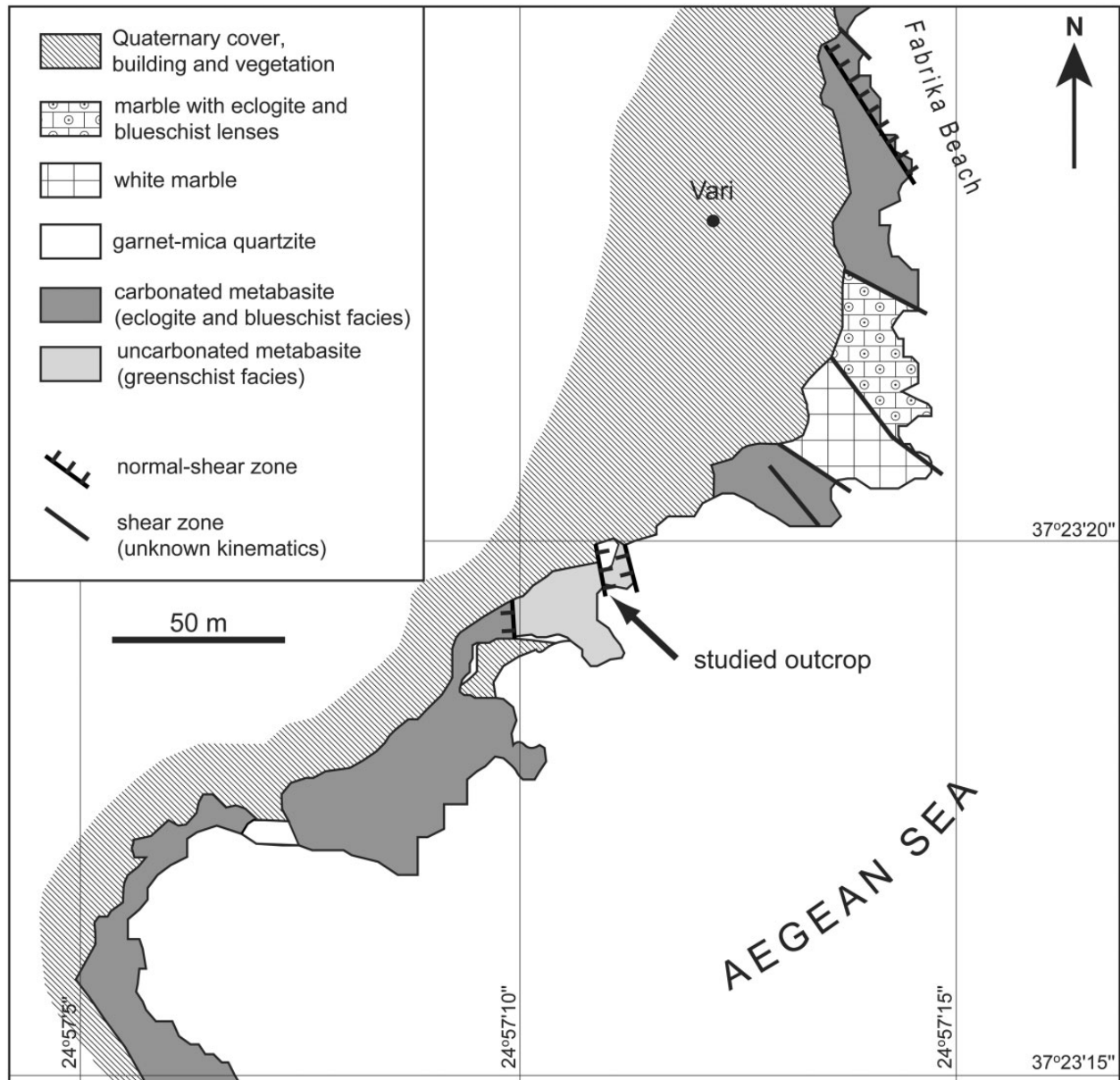


Fig. 2. Simplified geological map of Fabrika Beach close to the village of Vari (SE Syros).

colour changes along the profiles could be related to changes of bulk-rock chemistry. The trace element chemistry of all samples was determined following lithium-metaborate–tetraborate fusion by ion-coupled plasma mass spectrometry at Activation Laboratories in Canada. Precision was controlled through repeat analyses of international reference materials and is better than 1% and 5% for major and trace elements respectively. These data were used to help distinguish between metasomatism and isochemical fluid–rock interaction. The volatile content of all samples was measured as loss on ignition (LOI). Bulk-

rock CO_2 contents were determined using the field-based method of Skelton *et al.* (1995) called ‘fizz-o-metry’. For this method a small volume of crushed sample is reacted with HCl in a sealed vessel and the pressure of evolved CO_2 that is liberated during the reaction of HCl with carbonates gives the amount of calcite in the bulk-rock and therefore a value for the CO_2 content of the sample. The CO_2 value was then subtracted from the LOI value to obtain the H_2O content of the sample.

Mineral chemistry was determined using a JEOL JXA-8530 field emission electron microprobe (EMPA) at the

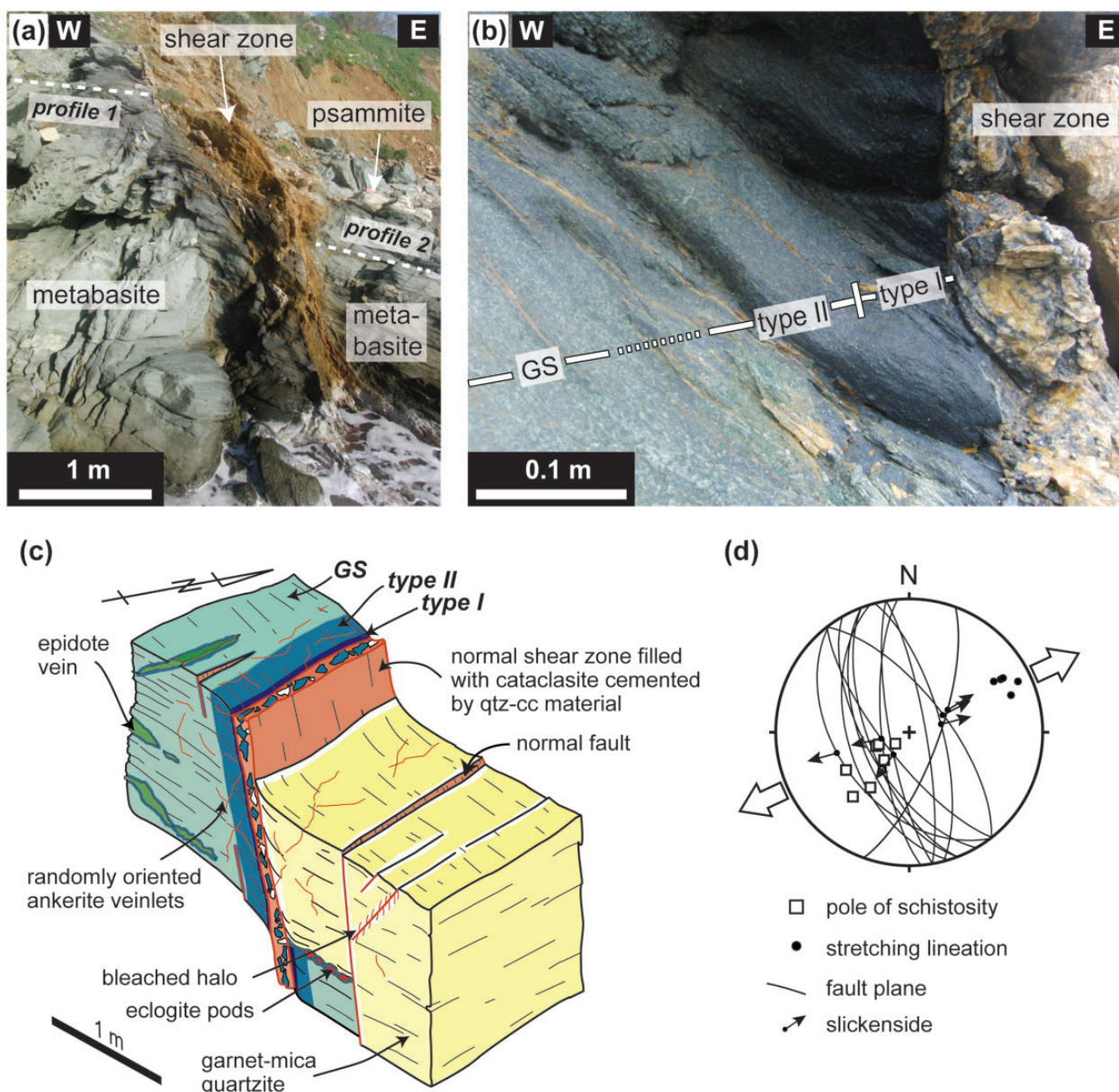


Fig. 3. (a) Field photograph showing the steeply dipping normal shear zone cutting through retrogressed greenschist-facies rocks at Fabrika Beach. A diffusive blue halo surrounds the shear zone. (b) Close-up view of the shear zone with type I and II blue haloes and surrounding greenschist (GS). (c) Schematic three-dimensional sketch of the outcrop showing that the blue halo continues on both sides of the normal shear zone within the greenschist-facies rocks. (d) Stereoplote showing the consistent direction of extension determined with both ductile and brittle structures.

Department of Earth Sciences, Uppsala University. JEOL PC-EMPA application software (version 1.5.0.4) was used and running conditions were 15 kV and 20 nA, with a beam size of 0.5–10 μm . Epidote, chlorite, albite, phengite, amphibole, garnet and carbonates were analyzed from representative samples from profiles 1 and 2 and the surrounding rocks. Thermodynamic modeling was performed using the computer program PerPlex 6.6.6 (Connolly, 1990, 2005, 2009) with the thermodynamic dataset HP02 (Holland & Powell, 1998).

PETROGRAPHY

Modal data are reported in Tables 1 and 2 and shown graphically in Fig. 4. Rock textures are shown in Figs 5–9.

Modal data

We compare modal data from samples collected along profiles 1 and 2 with those for representative greenschist- and blueschist-facies metabasites collected far from the shear zone.

Table 1: Mineral modes for samples from the shear zone and representative greenschist- and blueschist-facies metabasites

Domain:	Shear zone*	Representative greenschist	Representative blueschist
Sample:	50.9FB	13FB	24FB
Distance (m):	0.0	4.0	150.0
white mica	0.0	12.6	11.6
chlorite	5.0	17.1	1.2
glaucophane	10.0	0.0	41.1
actinolite	0.0	26.9	0.0
carbonates	15.0	0.4	17.6
albite	50.0	24.0	0.0
titanite	0.0	0.9	0.6
epidote	0.0	18.0	26.9
quartz	20.0	0.0	0.0
rutile	0.0	0.0	0.3
garnet	0.0	0.1	0.7

*Estimated values from field and thin-section observation.

Representative blueschist- and greenschist-facies metabasites

Modal data for representative blueschist- and greenschist-facies metabasites are listed in Table 1. The blueschist-facies metabasite sample contains $41.1 \pm 3.1\%$ glaucophane, $11.6 \pm 2.0\%$ phengite, $1.2 \pm 0.7\%$ chlorite, $26.9 \pm 2.8\%$ epidote, $17.6 \pm 2.4\%$ calcite and $0.7 \pm 0.5\%$ garnet. The greenschist-facies metabasite sample contains $26.9 \pm 2.8\%$ actinolite, $24.0 \pm 2.7\%$ albite, $17.1 \pm 2.4\%$ chlorite, $18.0 \pm 2.4\%$ epidote and $0.4 \pm 0.4\%$ calcite.

Profiles across the shear zone and its margins

Modal data from the shear zone and its margins are listed in Tables 1 and 2. The shear zone contains metamorphic minerals (quartz, albite, glaucophane, chlorite and calcite) and minerals filling late-stage veins (dolomite). The margins comprise type I and II blue haloes and greenschist-facies rocks. The boundaries between the zones are diffuse (Fig. 4). Profile 1 (SW side of shear zone) is well preserved, whereas the modal variation along profile 2 is largely obscured by post-metamorphic dolomitic veins that cross-cut the metamorphic foliation. The following description focuses on profile 1.

The type I blue halo contains 70–80% fine-grained (0.1–0.8 mm) prismatic crystals of glaucophane in an ultrafine-grained (0.1–0.2 mm) matrix of phengite and chlorite (Fig. 5a and b). Alignment of glaucophane, phengite and chlorite delineates a pervasive foliation (Fig. 5a). This foliation bends into the shear zone (Figs 3 and 5a).

In the type II blue halo, rocks contain large (up to 3.5 mm) porphyroblasts of albite and epidote in a fine-grained matrix that consists of varying amounts of amphibole, phengite, chlorite and calcite (Fig. 5c). Alignment of amphibole and phengite crystals delineates a pervasive foliation. Epidote porphyroblasts are aligned parallel to this foliation, whereas albite porphyroblasts overgrow this foliation. Minor amounts of garnet are also seen. The mode of amphibole in the type II blue haloes decreases from 40–50% close to the shear zone to ~30% further away. This amphibole is mainly glaucophane close to the shear zone but becomes rimmed and thereafter replaced by actinolite with increasing distance from the shear zone. This is coupled with an overall decrease in the modes of phengite and calcite from 20–30% close to the shear zone to 0–10% further away. The modes of epidote and albite increase from 0–5% close to the shear zone to 20–30% further away. The mode of chlorite increases from 10–20% close to the shear zone to 20–30% further away. The modal mineralogy of the type II blue halo sample collected closest to the shear zone (0.3-1FB) is similar to that of a representative blueschist-facies metabasite collected far from the shear zone, except for chlorite and epidote (Tables 1 and 2).

The surrounding greenschist-facies rocks contain porphyroblasts of albite and epidote in a fine-grained matrix that is mostly composed of actinolite and chlorite (Fig. 5d). The mode of actinolite is 10–20%. The modes of epidote, chlorite and albite are 20–30%. Only traces of calcite and phengite are observed in the greenschist-facies rocks. The modal mineralogy of greenschist-facies rocks surrounding the shear zone is similar to that of representative greenschist-facies metabasite collected far from the shear zone (Tables 1 and 2).

Rock textures

Foliation, porphyroblasts and reaction textures can be used to elucidate a metamorphic history for the rocks in our study area.

Foliation

Foliation in the blue haloes is well defined by the preferred alignment of glaucophane (which is partly replaced by actinolite in the type II halo) and phengite (Fig. 5a–c). This implies that the rock became foliated during or after growth of glaucophane and phengite. Foliation intensity in the blue haloes increases towards the shear zone and is deflected so as to become parallel to it (Figs 3 and 5a). This most probably implies that the shear zone was formed at the same time as, or after, the rock was foliated. Foliation in the surrounding greenschist-facies rocks is less well defined. Epidote and phengite, which are derived from the HP–LT mineral assemblage, are aligned, whereas chlorite crystals are mostly randomly oriented (Fig. 5d).

Table 2: Mineral modes from profiles 1 and 2

Domain:	Profile 1							
	Type I blue halo	Type II blue halo				Greenschist		
	Sample:	0.05-1FB	0.2-1FB	0.3-1FB	0.4-1FB	0.5-1FB	0.7-1FB	0.9-1FB
Distance (m):	0.05	0.2	0.3	0.4	0.5	0.7	0.9	1.2
white mica	4.1	24.9	13.6	18.2	16.2	2.9	7.0	4.0
chlorite	7.8	17.5	15.3	10.8	11.6	26.6	24.3	17.2
glaucophane	83.2	45.3	43.6	37.1	30.5	9.2	6.7	7.4
actinolite	0.0	0.0	0.0	0.0	9.1	11.4	14.9	17.4
carbonates	0.2	9.7	19.3	23.6	13.5	14.5	4.5	1.7
albite	0.0	0.7	4.4	5.9	9.9	25.1	19.7	20.4
titanite	3.4	1.0	1.2	2.1	1.8	2.2	2.0	4.1
epidote	0.8	0.1	1.8	2.2	5.8	7.9	20.1	26.7
quartz	0.5	0.8	0.8	0.1	1.6	0.4	0.1	1.1

Domain:	Profile 2							
	Type I blue halo	Type II blue halo		Greenschist				
	Sample:	0.1-2FB	0.2-2FB	0.25-2FB	0.3-2FB	0.35-2FB	0.4-2FB	0.6-2FB
Distance (m):	0.1	0.2	0.25	0.3	0.35	0.4	0.6	0.9
white mica	5.7	8.3	4.7	2.8	3.2	1.9	0.9	3.2
chlorite	6.2	10.0	13.0	27.3	27.6	22.1	19.5	23.0
glaucophane	57.5	43.0	53.0	24.0	19.0	20.3	27.5	4.9
actinolite	0.0	0.0	0.0	0.7	1.6	2.5	11.2	4.9
carbonates	22.1	26.4	6.8	11.8	16.9	17.4	2.3	16.3
albite	3.5	8.8	18.5	24.6	19.5	29.1	19.8	35.4
titanite	4.1	2.6	2.2	3.9	3.9	1.5	5.0	3.1
epidote	0.2	0.0	1.6	4.8	7.6	4.1	11.7	8.7
quartz	0.7	0.9	0.2	0.1	0.9	1.0	2.0	0.6

This implies that chlorite grew after the rock became foliated.

Porphyroblasts

Epidote and albite occur as porphyroblasts in the type II blue halo and surrounding greenschist-facies rocks. Epidote porphyroblasts are aligned, elongated and pulled apart into segments parallel to this foliation (Fig. 6d). This implies that the epidote porphyroblasts formed before or at the same time as the rock was foliated. In contrast, porphyroblasts of albite overgrow the foliation. Inclusion trails within these porphyroblasts are sigmoidal and continuous with the foliation in the surrounding rock. This implies that the albite porphyroblasts grew towards the

end of the time during which the rock was becoming foliated.

Reaction textures

In this subsection, we present textural evidence for (1) metasomatism, (2) carbonation and (3) retrograde decarbonation and the relative timing of these stages.

(1) Metasomatism. Textural evidence of metasomatism is seen in only the type I blue halo. The fine-grained matrix of this halo mostly comprises glaucophane with minor amounts of phengite (Fig. 5b). In Fig. 6a, euhedral and subhedral crystals of glaucophane are seen replacing a larger phengite crystal. Furthermore, we observe skeletal epidote that is surrounded by a very fine-grained phase

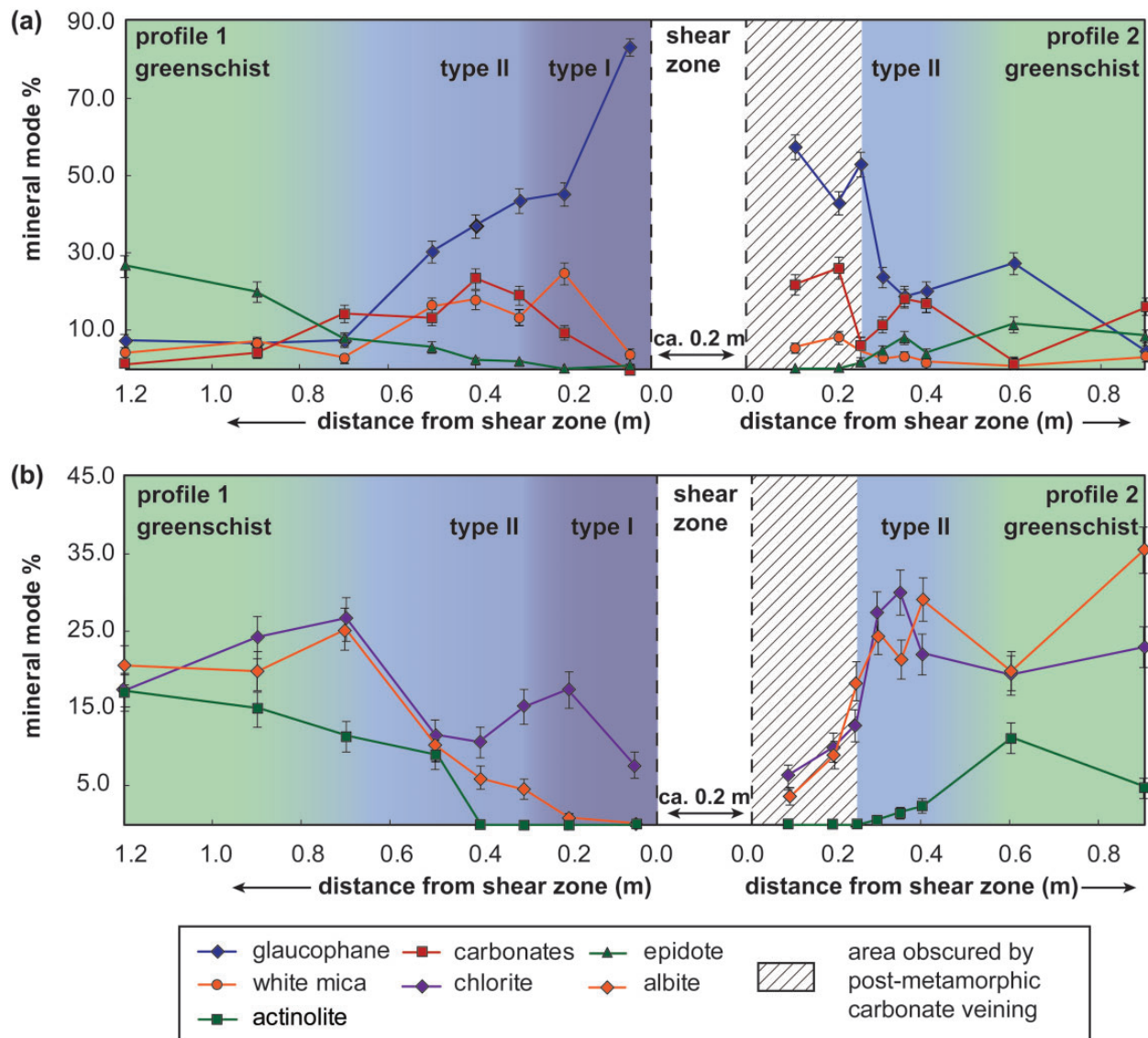


Fig. 4. Mineral modes along profiles 1 and 2. The two types of blue halo and the greenschist can be clearly distinguished by the change in mineralogy. (a) Mineral modes of glaucophane, white mica, epidote and carbonate. (b) Mineral modes of chlorite, actinolite and albite.

with optical properties similar to those of white mica (Fig. 6b). Electron microprobe analysis of this phase (Table 3) shows that its composition is intermediate between those of pyrophyllite and celadonite, with small amounts of paragonite and trioctahedral mica. These mineral replacement textures could imply loss of some major elements (e.g. K, Ca) and gain of other major elements (e.g. Na).

(2) Carbonation. Textural evidence of carbonation is largely restricted to the type II blue halo. The foliated matrix comprises glaucophane, phengite and calcite with porphyroblasts of epidote and albite (Fig. 5c). Both glaucophane and epidote crystals are partially replaced by calcite. Glaucophane crystals are partly pseudomorphed by

calcite, which grows along cleavages and fractures (Fig. 6c). Calcite fills open spaces between pulled-apart segments of elongated epidote crystals (Fig. 6d). This observation implies that calcite grew at the same time as the epidote crystal was being pulled apart; that is, carbonation occurred while the foliation was developing. These mineral replacement textures imply addition of CO_2 .

(3) Retrograde decarbonation. Textural evidence of retrogression at greenschist-facies conditions is seen in the type II blue halo further from the shear zone and in the surrounding greenschist-facies rocks. The most important evidence is that back-scattered electron (BSE) images reveal that glaucophane is rimmed by actinolite (Fig. 7). Other evidence of retrogression includes replacement of

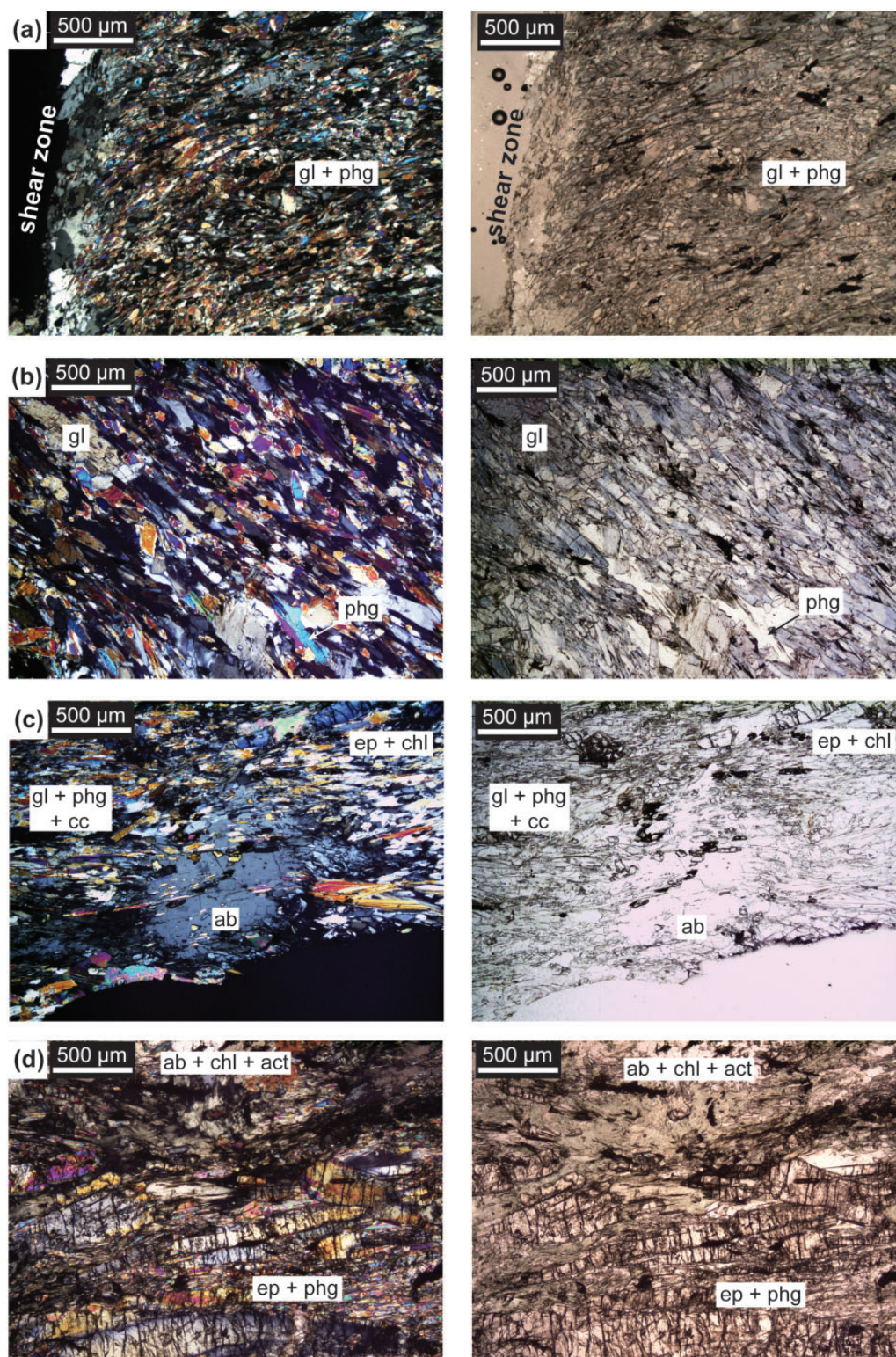


Fig. 5. Photomicrographs of thin sections from the two types of halo and the greenschist. Left panels under crossed polars; right panels under plane polars. (a) Type I halo at low magnification. The foliation, which is defined by glaucophane (gl) and phengite (phg), bends into the shear zone. (b) Fine-grained matrix of the type II blue halo, which mostly comprises glaucophane and phengite. (c) Type II halo at low magnification. This rock comprises a foliated matrix of glaucophane, phengite and calcite (cc) with porphyroblasts of epidote and albite. The albite porphyroblasts overgrow the foliation. (d) The surrounding greenschist at low magnification. Epidote (ep) and phengite, which derive from an HP–LT mineral assemblage, are aligned whereas chlorite (chl), actinolite (act) and albite (ab) overgrow the foliation.

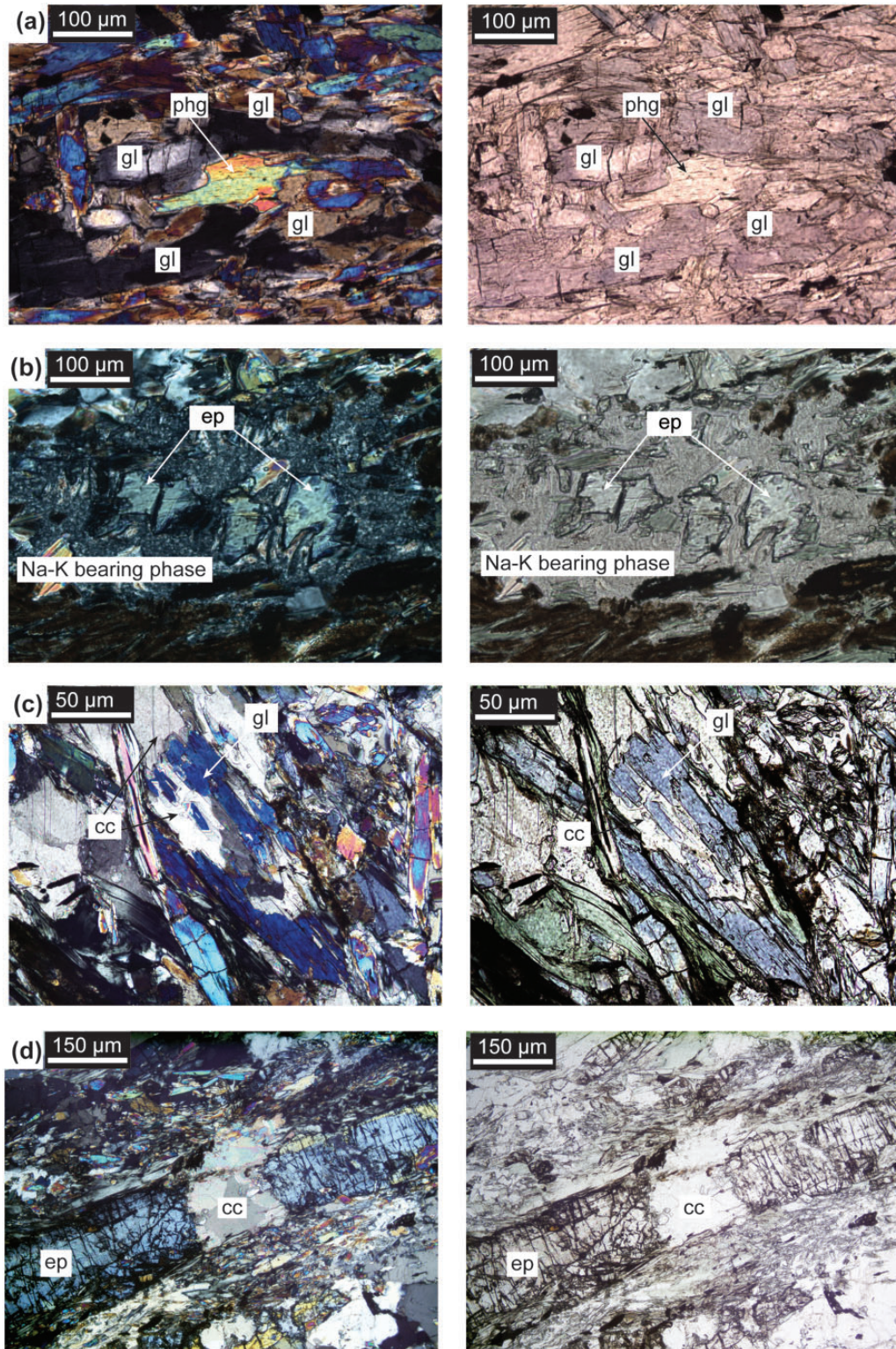


Fig. 6. Photomicrographs of reaction textures in the type I and type II haloes. (a) Metasomatic replacement of phengite by glaucophane in the type I halo. (b) Epidote breaking down to an Na–K-bearing phase in the type I blue halo. (c, d) Carbonation of an original blueschist mineral assemblage in the type II halo in which glaucophane and epidote are replaced by calcite. Left panels under crossed polars; right panels under plane polars.

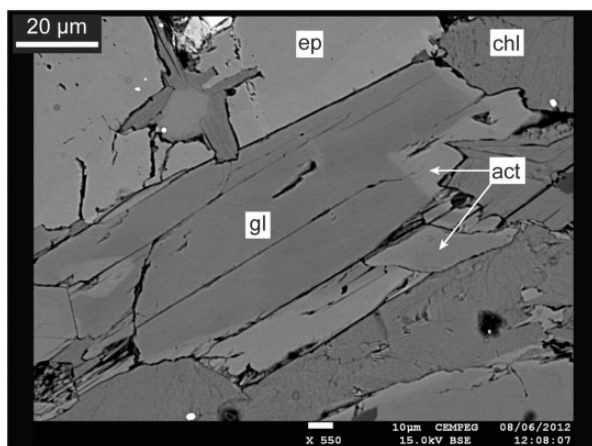


Fig. 7. Back-scattered electron (BSE) image of the type II blue halo showing glaucophane that is replaced by actinolite at its rim.

glaucophane by chlorite and albite (Fig. 8a) and pseudomorphic replacement of phengite and garnet by chlorite (Fig. 8b and c). Retrogression was accompanied by decarbonation. This can be seen in Fig. 9, which shows several examples where skeletal crystals of albite grow along grain boundaries between reactant minerals. In Fig. 9a a skeletal albite crystal has nucleated on phengite crystals and grows along boundaries between calcite crystals. In Fig. 9b a glaucophane crystal that is partly pseudomorphed by calcite is partly replaced by albite, which grows at the boundary between glaucophane and calcite. In each of Fig. 9c and d calcite filling an open space between pulled-apart segments of an epidote is partly replaced by albite. In both examples, a skeletal albite crystal has nucleated on the epidote crystal and grows along boundaries between calcite crystals.

Metamorphic history

In summary, blueschist-facies rocks were first carbonated during foliation development and thereafter retrogressed at greenschist-facies conditions. Further evidence that carbonation preceded retrogression is seen in Fig. 9. This figure shows several examples of albite replacing previously carbonated assemblages. These textures not only imply that retrogression postdated carbonation but also that CO_2 was lost during retrogression; that is, the blueschist-facies rocks were first carbonated and then subsequently decarbonated.

We cannot unequivocally ascertain the relative timing of metasomatism in the type I blue halo. Glaucophane crystals produced by the breakdown of phengite are aligned parallel to the foliation, which could imply that metasomatism occurred before or at the same time as the foliation developed. However, we cannot exclude the possibility that metasomatism occurred later and that the

newly formed glaucophane crystals mimic a pre-existing foliation.

GEOCHEMISTRY

Whole-rock chemical data with oxides reported as wt % on a volatile-free basis are listed in Tables 4 and 5 and shown graphically in Figs 10 and 11. Mineral chemical data are listed in Tables 6 and 7 and shown graphically in Figs 12 and 13.

Whole-rock chemistry

In this section, we compare whole-rock chemical data from samples collected along profiles 1 and 2 with representative greenschist- and blueschist-facies metabasites collected far from the shear zone.

Representative blueschist- and greenschist-facies metabasites

Major element data and trace element data for representative blueschist- and greenschist-facies metabasites are given in Table 4. These rocks are similar to basalt in terms of their major element chemistry. The volatile contents (H_2O and CO_2) are generally lower in the greenschist than in the blueschist. The higher CO_2 content (5.0 wt %) of the blueschist-facies metabasite reflects its high carbonate content (Table 1).

Profiles across the shear zone and its margins

Major element data and trace element data from the margins of the shear zone are given in Table 5. We focus our discussion on profile 1 because it is not obscured by post-metamorphic dolomite veins.

Samples from the type I blue halo contain higher concentrations of SiO_2 and Na_2O and lower concentrations of Al_2O_3 , CaO , MnO and volatiles (H_2O and CO_2) compared with the continuation of the profile (Table 5) and the representative blueschist-facies metabasite (Table 4). Samples from the type II blue halo are similar to the representative blueschist-facies metabasite on a volatile-free basis (Table 4). They are also similar to the surrounding greenschist-facies rocks with the exception of K_2O , which occurs in higher concentrations in the type II blue halo. The CO_2 content of the type II blue halo is greater than in both the type I halo and the surrounding greenschist-facies rocks. This reflects the high carbonate content of these samples (Table 2).

We use concentration ratios and isocon diagrams to investigate major and trace element variation along profiles 1 and 2 (Figs 10 and 11). For construction of the diagrams constant volume was assumed, based on the occurrence of pseudomorphic replacement textures (see Figs 7 and 8) and similar rock densities ($2.6\text{--}2.7\text{ g cm}^{-3}$) for type I, type II blue halo and the greenschist. For the concentration ratios the three last samples of each profile were chosen as the precursor rock composition, as these samples were

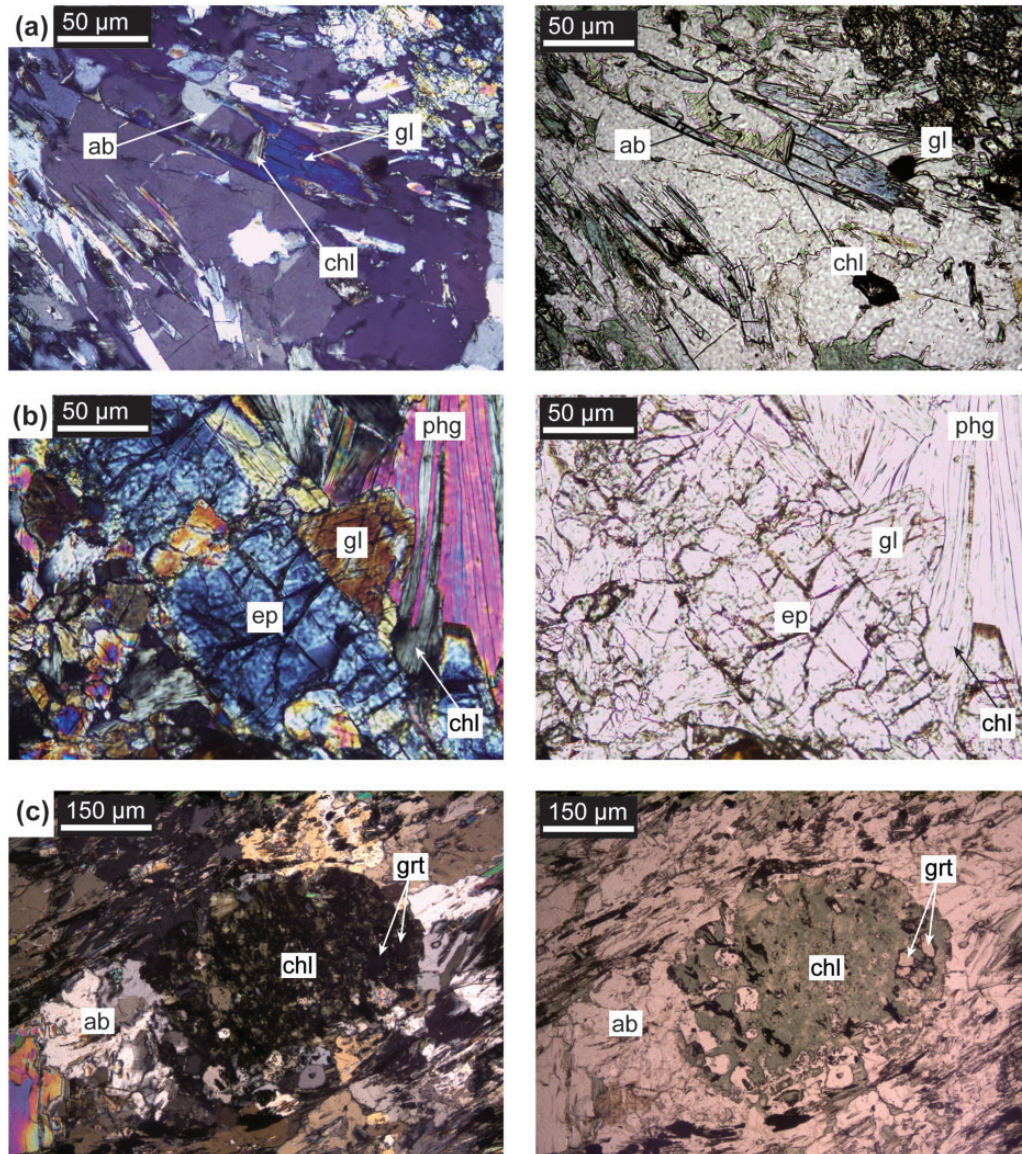


Fig. 8. Photomicrographs illustrating retrogression of the carbonated blueschist in the type II halo and parts of the greenschist. (a) Glaucophane is partly replaced by albite + chlorite. (b) Glaucophane is partly replaced by epidote and phengite is partly replaced by chlorite. (c) Nearly complete replacement of garnet (grt) by chlorite. Left panels under crossed polars; right panels under plane polars.

considered to be those least affected by any metasomatic overprint. For the isocon diagrams we compare the average concentration of each type of blue halo with the average concentrations of samples from greenschist-facies rocks collected along the profiles. Both profiles are presented, but in the following description, we focus on profile 1 (footwall) because this profile is largely free from post-metamorphic dolomite veins. Chemical variability along profile 2 partly reflects vein densities and is therefore less useful as a record of metamorphic processes.

Concentration ratio diagrams (Fig. 10) can provide evidence that mass change has occurred. Here, we use such

diagrams to assess the extent to which formation of the type I and II blue haloes can be attributed to metasomatic processes. Major and trace elements have been normalized to Ti, which is considered to be the least mobile element following the statistical approach of Ague & van Haren (1996). Normalizing to Ti eliminates primary compositional variation and allows us to observe true mass changes during metamorphic and/or metasomatic events. Mass-balance calculations were carried out following Ague (2003b) and references therein. This analysis shows that the type I blue halo along profile 1 is enriched in SiO₂ and Na₂O (Fig. 10a), LILE (Fig. 10b) and high field

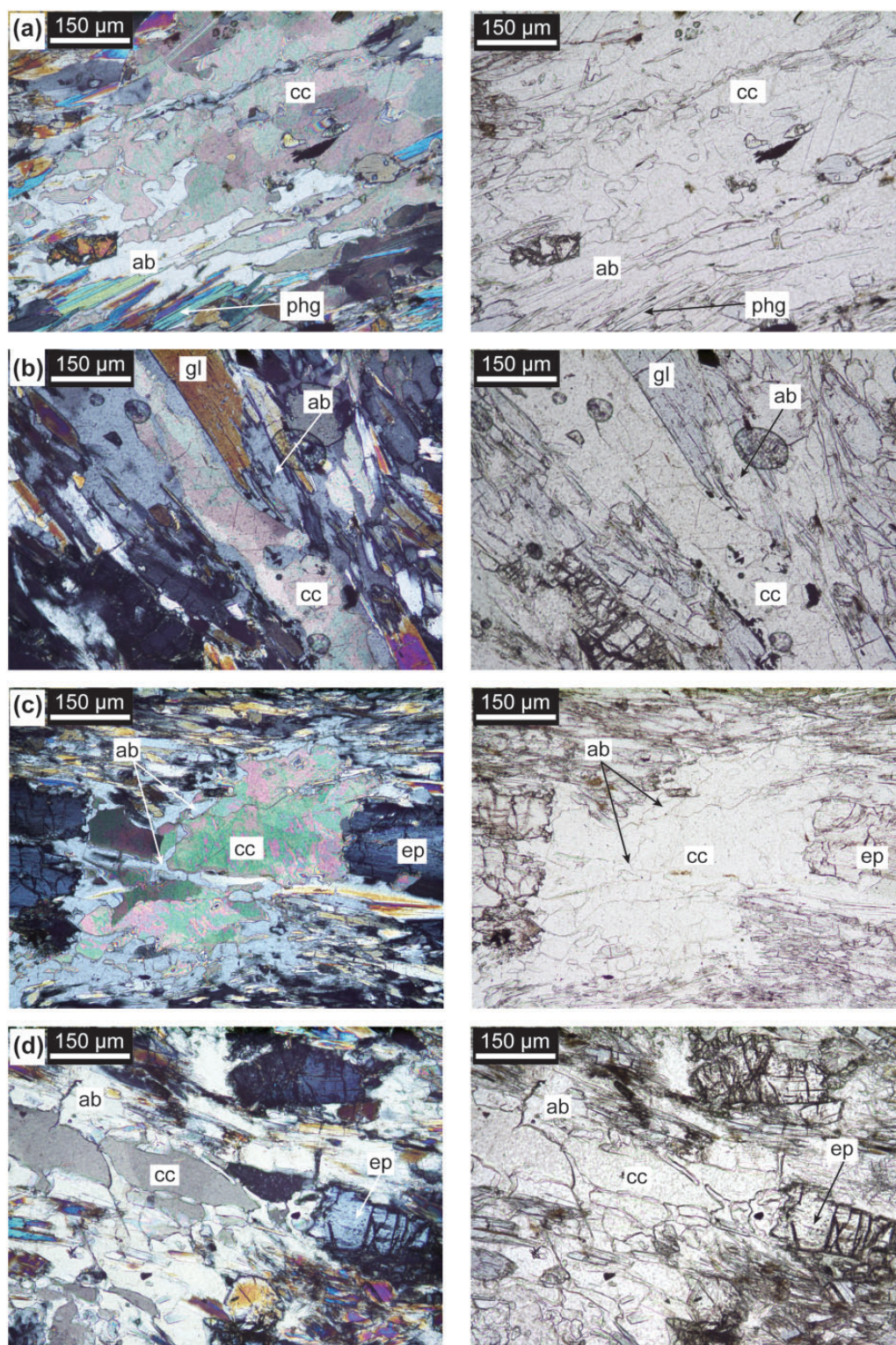


Fig. 9. Photomicrographs of the type II halo and the surrounding greenschist. (a, b) Albite growth along grain boundaries at the expense of phengite, glaucophane and calcite. (c, d) Prismatic crystals of epidote that have been partly replaced by calcite. These partly replaced crystals are overgrown by albite along grain boundaries and fractures. Left panels under crossed polars; right panels under plane polars.

Table 3: Composition of the Na–K-bearing phase that replaces epidote in the type I halo

Domain:	Type I halo
Mineral:	Na–K-bearing phase
Sample:	0.1-2FB
SiO ₂	55.82
TiO ₂	0.12
Al ₂ O ₃	23.42
FeO(tot)	4.70
Cr ₂ O ₃	0.01
MgO	2.83
MnO	0.00
CaO	0.26
Na ₂ O	1.12
K ₂ O	4.35
Total	92.63

strength elements (HFSE) (Fig. 10c), but depleted in CaO, MnO (Fig. 10a and b), rare earth elements (REE) (Fig. 10d) and volatiles (Fig. 10e) compared with the surrounding greenschist-facies rocks. The analysis also shows that the type II blue halo along profile 1 is chemically similar to the surrounding greenschist-facies rocks, with the exception of the LILE, which are enriched (Fig. 10b). Given the high mobility of the LILE, we thus conclude that metasomatism played only a minor role in the formation of the type II blue haloes. The CO₂ content (Fig. 10e) reaches a maximum at the boundary between the type I and II blue haloes.

Isocon diagrams (Grant, 1986) can provide further evidence that mass change has occurred (Fig. 11). Here, we use these to assess the extent to which formation of the type I and II blue haloes occurred by metasomatic processes. In Fig. 11a, in which the type I blue halo is compared with the surrounding greenschist-facies rocks, SiO₂, Na₂O and K₂O plot above the 1:1 reference line, whereas CaO, MnO and CO₂ plot below this line. In Fig. 11c, which compares the type II blue halo with the surrounding greenschist-facies rocks, K₂O (which belongs to the highly mobile LILE) and the CO₂ content plot above the 1:1 reference line. All other major components plot close to this line.

In summary, rocks in the type I blue halo are chemically different from the surrounding greenschist-facies rocks whereas rocks in the type II blue halo are chemically similar to the surrounding greenschist-facies rocks. We thus infer that metasomatism was largely restricted to the type I blue halo. The only exceptions are the mobile elements

Table 4: Whole-rock major and trace element chemistry for representative greenschist-facies and blueschist-facies metabasites

Domain:	Representative greenschist	Representative blueschist
Sample:	13FB	24FB
Distance (m):	4.0	150.0

Major elements (wt %)

SiO ₂	50.0	47.2
Al ₂ O ₃	16.0	16.0
Fe ₂ O _{3(tot)} *	9.0	11.0
MnO	0.2	0.2
MgO	10.9	7.5
CaO	9.1	12.4
Na ₂ O	2.6	3.6
K ₂ O	1.2	1.4
TiO ₂	0.8	0.7
P ₂ O ₅	0.3	0.1
H ₂ O	1.5	2.4
CO ₂	2.4	5.0

Trace elements (ppm)

V	239	290
Rb	26	26
Sr	288	136
Zr	73	29
Nb	4.9	<0.2
Cs	0.8	1.4
Ba	349	145
La	21	13
Ce	44	23
Pr	5.1	2.6
Nd	20	9
Sm	4.2	2.1
Eu	1.2	0.7
Gd	3.9	2.1
Tb	0.6	0.3
Dy	3.4	2.0
Ho	0.6	0.4
Er	1.7	1.2
Tm	0.2	0.2
Yb	1.6	1.2
Lu	0.3	0.2
Hf	1.6	0.8
Ta	0.4	0.1
Th	4.6	4.4
U	1.0	0.9

*Fe₂O_{3(tot)} = total iron.

Oxides are reported on a volatile-free basis.

Table 5: Whole-rock major and trace element chemistry for profiles 1 and 2

Domain:	Profile 1							
	Type I blue halo	Type II blue halo				Greenschist		
Sample:	0.05-1FB	0.2-1FB	0.3-1FB	0.4-1FB	0.5-1FB	0.7-1FB	0.9-1FB	1.2-1FB
Distance (m):	0.1	0.2	0.3	0.4	0.5	0.7	0.9	1.2
<i>Major elements (wt %)</i>								
SiO ₂	56.7	52.8	48.2	48.6	49.4	49.7	50.1	50.3
Al ₂ O ₃	13.7	16.3	15.6	16.2	16.7	16.9	17.1	16.4
Fe ₂ O _{3(tot)} *	10.2	9.5	8.9	8.3	8.1	8.3	8.2	9.4
MnO	0.1	0.1	0.2	0.1	0.1	0.2	0.1	0.2
MgO	9.6	9.7	10.5	9.5	9.2	9.4	9.6	10.0
CaO	1.2	3.4	9.9	10.2	9.4	9.2	9.7	8.8
Na ₂ O	5.5	3.9	3.5	3.8	4.0	4.6	3.4	3.1
K ₂ O	2.0	3.1	2.3	2.2	2.0	0.6	0.8	0.8
TiO ₂	0.8	0.8	0.8	0.8	0.9	0.9	0.9	0.8
P ₂ O ₅	0.2	0.2	0.2	0.3	0.2	0.3	0.2	0.2
H ₂ O	0.2	2.8	1.1	3.2	1.5	2.0	1.5	1.3
CO ₂	2.4	2.6	8.1	5.7	6.4	5.0	3.5	2.6
<i>Trace elements (ppm)</i>								
V	246	215	200	206	213	218	221	216
Rb	47	70	50	47	44	13	18	17
Sr	13	73	214	233	226	230	251	230
Zr	82	71	64	70	74	74	77	73
Nb	7.4	6.3	5.8	6.5	6.9	7.7	7.2	6.8
Cs	2.6	4.3	2.6	2.4	2.1	0.7	0.8	0.8
Ba	415	593	425	420	400	133	195	191
La	21	17	18	22	22	21	22	21
Ce	46	37	39	45	46	45	47	44
Pr	5.0	4.2	4.6	5.1	5.2	5.3	5.3	5.0
Nd	20	17	18	21	21	21	22	21
Sm	3.7	3.5	4.0	4.3	4.4	4.6	4.5	4.4
Eu	0.9	0.9	1.2	1.2	1.3	1.4	1.3	1.3
Gd	3.0	3.0	3.5	3.9	3.9	4.1	4.0	3.9
Tb	0.4	0.4	0.5	0.6	0.6	0.6	0.6	0.6
Dy	2.3	2.3	3.0	3.2	3.2	3.4	3.0	3.3
Ho	0.4	0.4	0.6	0.6	0.6	0.6	0.6	0.6
Er	1.2	1.2	1.5	1.7	1.8	1.8	1.7	1.7
Tm	0.2	0.2	0.2	0.2	0.3	0.3	0.2	0.3
Yb	1.2	1.2	1.5	1.6	1.6	1.6	1.6	1.6
Lu	0.2	0.2	0.2	0.3	0.3	0.3	0.3	0.3
Hf	1.5	1.4	1.0	1.3	1.3	1.4	1.4	1.3
Ta	0.3	0.4	0.2	0.3	0.3	0.4	0.4	0.4
Th	5.5	4.4	3.9	4.4	4.5	4.6	4.9	4.6
U	1.6	1.5	0.9	1.1	1.1	1.1	1.2	1.2

(continued)

Table 5: Continued

Domain:	Profile 2							
	Type I blue halo	Type II blue halo		Greenschist				
Sample:	0.1-2FB	0.2-2FB	0.25-2FB	0.3-2FB	0.4-2FB	0.4-2FB	0.6-2FB	0.9-2FB
Distance (m):	0.1	0.2	0.3	0.3	0.4	0.4	0.6	0.9
<i>Major elements (wt %)</i>								
SiO ₂	42.8	49.0	55.3	50.7	51.5	51.4	53.1	49.2
Al ₂ O ₃	15.9	16.3	15.7	17.9	18.1	17.7	17.2	18.7
Fe ₂ O _{3(tot)} *	8.1	8.0	8.3	7.8	7.7	7.4	7.1	8.0
MnO	0.2	0.1	0.1	0.1	0.1	0.1	0.1	0.2
MgO	8.0	7.4	7.5	7.3	6.5	6.4	6.8	7.3
CaO	16.1	10.1	4.4	8.0	7.8	8.8	8.8	9.2
Na ₂ O	2.3	3.2	4.4	5.0	5.5	5.2	3.9	4.8
K ₂ O	3.7	4.3	2.3	1.2	1.0	1.4	1.5	0.8
TiO ₂	1.3	1.4	1.7	1.7	1.5	1.4	1.4	1.6
P ₂ O ₅	1.6	0.2	0.2	0.2	0.3	0.3	0.1	0.3
H ₂ O	5.0	5.4	4.3	1.3	2.3	1.8	2.2	1.7
CO ₂	10.1	7.5	3.3	7.0	6.1	6.4	3.1	5.5
<i>Trace elements (ppm)</i>								
V	194	208	227	234	210	218	238	238
Rb	67	84	47	24	21	27	30	15
Sr	84	42	54	247	244	264	366	308
Zr	100	124	149	136	133	132	127	143
Nb	11.1	13.7	16.3	15.3	14.1	12.6	13.9	15.3
Cs	3.3	4.3	4.0	0.9	1.9	1.4	1.6	0.4
Ba	820	715	366	269	173	213	280	189
La	12	10	8	11	10	11	13	13
Ce	28	25	27	28	25	27	32	32
Pr	3.8	3.3	2.6	3.6	3.2	3.4	4.1	4.1
Nd	17	14	11	16	14	15	18	18
Sm	4.2	3.5	2.8	3.8	3.4	3.7	4.4	4.3
Eu	1.4	1.1	0.9	1.3	1.1	1.2	1.5	1.4
Gd	4.5	3.4	2.7	3.9	3.3	3.7	4.3	4.3
Tb	0.8	0.6	0.4	0.7	0.7	0.6	0.7	0.8
Dy	4.9	3.7	2.6	4.2	4.3	3.9	3.2	4.5
Ho	1.0	0.7	0.5	0.8	0.9	0.8	0.6	0.9
Er	2.8	2.1	1.5	2.2	2.4	2.1	1.5	2.4
Tm	0.4	0.3	0.2	0.3	0.4	0.3	0.2	0.4
Yb	2.8	2.2	1.5	2.2	2.4	2.0	1.4	2.4
Lu	0.5	0.4	0.2	0.4	0.4	0.3	0.2	0.4
Hf	1.8	2.2	2.8	2.3	2.3	2.4	2.2	2.5
Ta	0.8	0.9	1.2	1.0	1.0	1.0	1.0	1.1
Th	1.6	1.6	1.8	1.6	1.7	1.8	1.7	1.9
U	1.1	1.1	0.9	0.4	0.6	0.5	0.5	0.5

*Fe₂O_{3(tot)} = total iron.

Oxides are reported on a volatile-free basis.

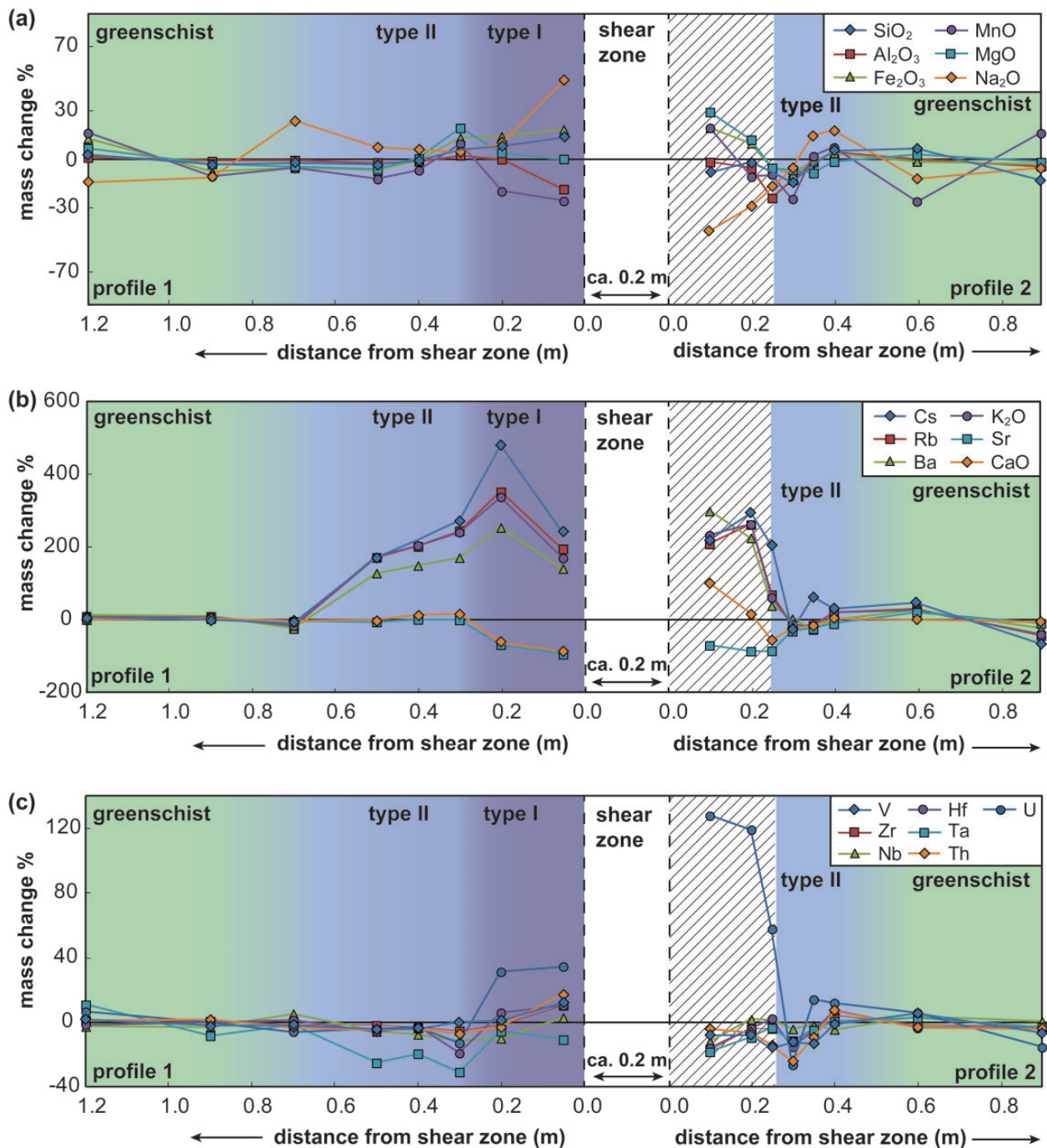


Fig. 10. Mass change in per cent along profiles 1 and 2 for major and trace elements. (a) Major elements (SiO₂, Al₂O₃, Fe₂O₃, MnO, MgO, Na₂O); (b) LILE (K₂O, Rb, Cs, CaO, Sr, Ba); (c) HFSE (V, Zr, Nb, Hf, Ta, Th, U); (d) REE (La, Ce, Pr, Nd, Sm, Eu, Gd, Tb, Dy, Ho, Er, Tm, Yb, Lu); (e) H₂O and CO₂. Elements with negative values are depleted in comparison with the reference element Ti, which is assumed to be immobile. Elements with positive values are enriched compared with Ti. The elements are normalized to the average elemental composition of the last three samples within the greenschist of the profiles, which are assumed to be least affected by metasomatism. The diagonally shaded areas show the regions that are affected by post-metamorphic veins.

(continued)

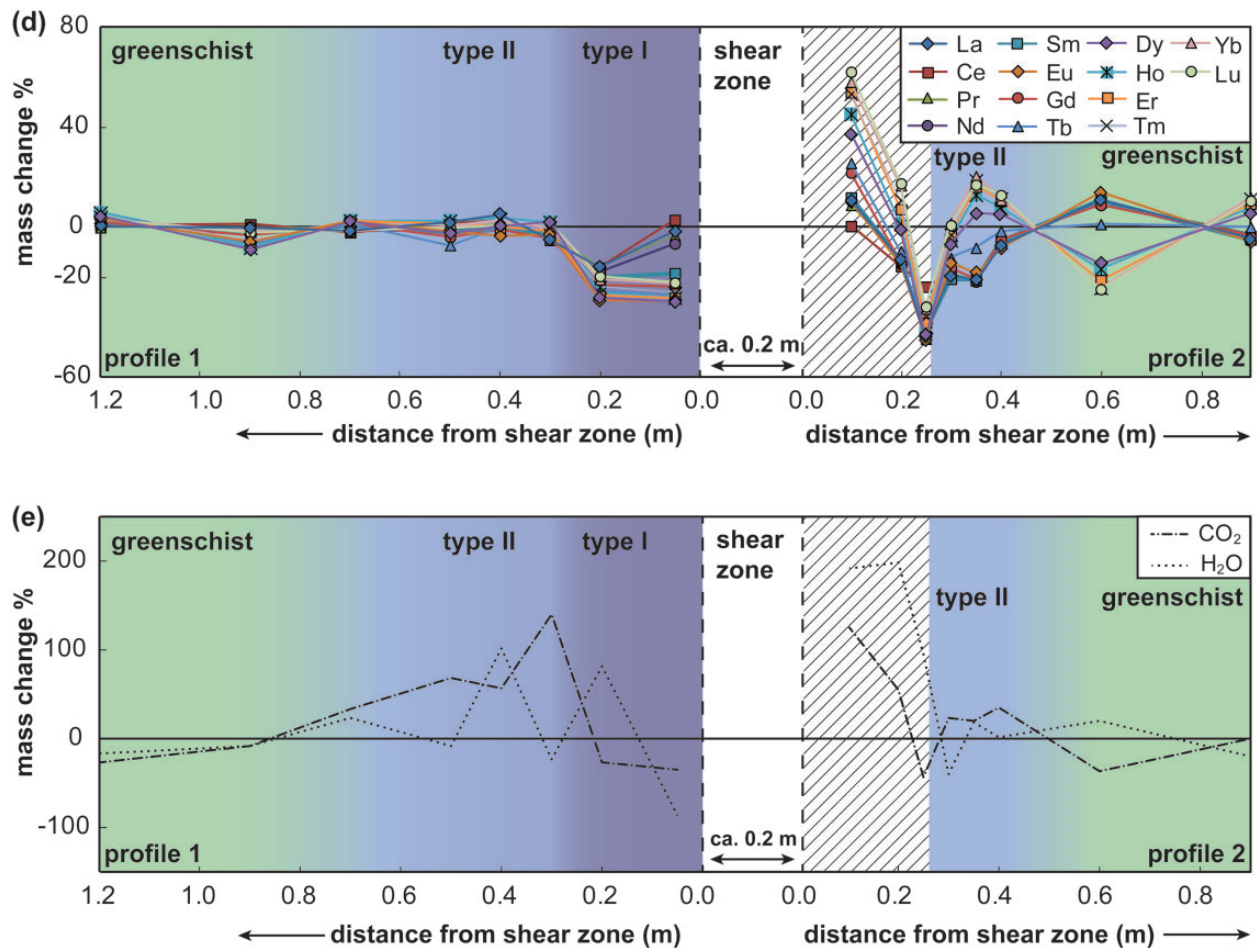


Fig. 10. Continued

(LILE including K), which are enriched in the type II blue halo. The concentration of CO₂ in the type II blue halo decreases as the extent of greenschist-facies retrogression increases with distance from the shear zone. This corroborates the textural evidence that retrogression at greenschist-facies conditions involved decarbonation of previously carbonated blueschist-facies rocks.

Mineral chemistry

Mineral chemistry data are reported for samples collected from representative greenschist- and blueschist-facies metabasites (Table 6) and from samples from profiles 1 and 2 (Table 7). Below we review evidence of chemical variability along these profiles for epidote, chlorite, plagioclase, phengite, amphibole, garnet and carbonates.

Epidote

Epidote compositions are reported as X_{cz} in Tables 6 and 7, where $X_{cz} = (Al - 2)/(Al + Fe^{3+} + Cr^{3+} - 2)$ (after Franz & Liebscher, 2004). In the type I blue haloes, epidote occurs in small quantities with $X_{cz} = 0.49$. In the type II

blue haloes and in the greenschist from the profiles epidote grains are usually zoned with Fe-depleted cores and Fe-enriched rims (Table 7). Epidotes from representative blueschist-facies and greenschist-facies metabasites show a similar zonation pattern with higher X_{cz} in the cores and lower X_{cz} in the rims (Table 6). However, epidote grains from representative greenschist-facies samples show a general decrease in the X_{cz} content.

Chlorite

There is little variation in chlorite composition along the profiles with Si (a.p.f.u.) ~ 2.8 – 2.9 and X_{Mg} [$Mg/(Fe + Mg)$] ~ 0.6 (Table 7). In comparison with chlorite from representative greenschist- and blueschist-facies metabasites, the Fe content is significantly higher within chlorite from the profiles (Table 6).

Plagioclase

There is no variation in plagioclase composition along the profiles, with $X_{ab} = 0.99$. This is as expected for

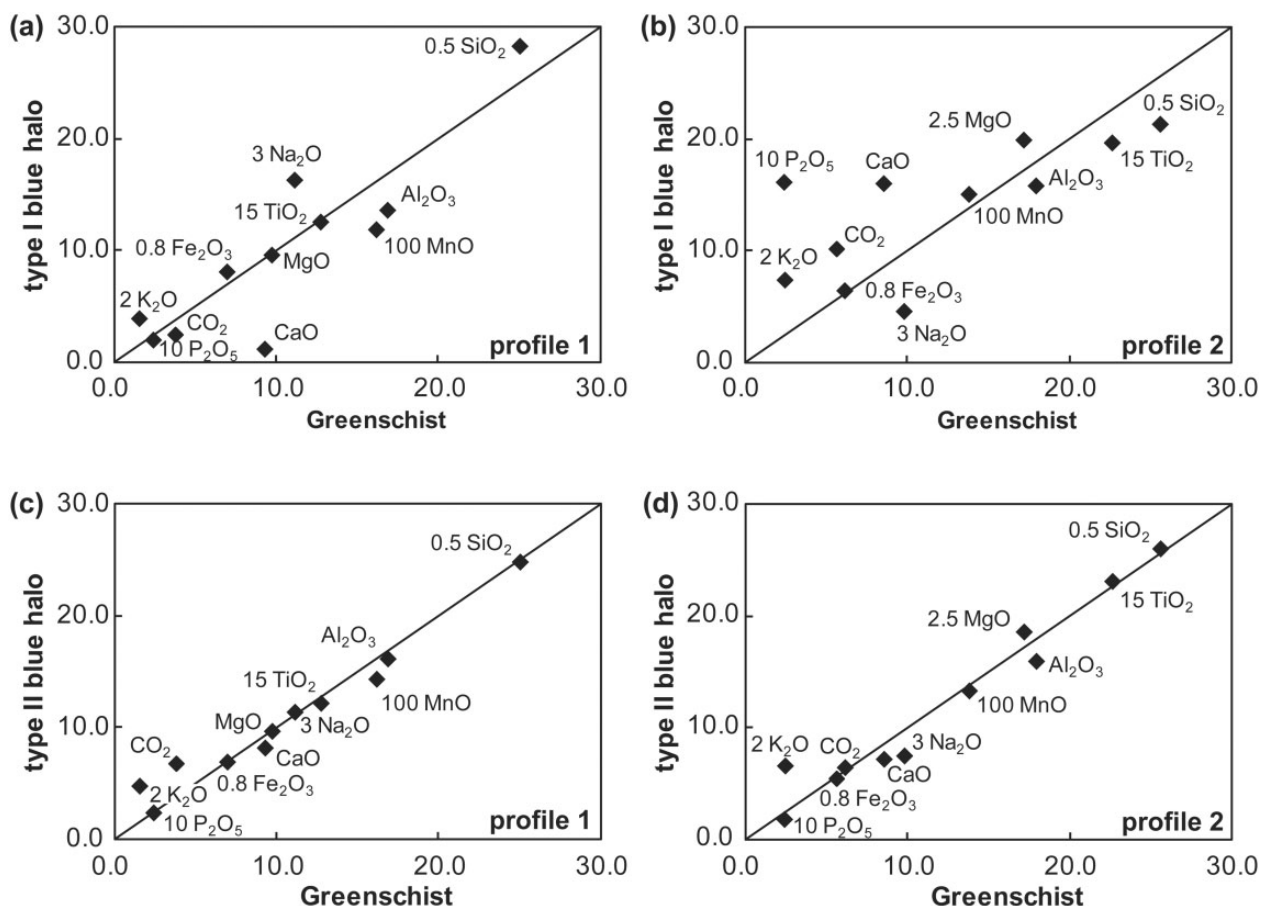


Fig. 11. Isocon diagrams for profiles 1 and 2 using average concentrations in the type I and type II blue haloes and the greenschist. (a) Profile 1 type I blue halo vs greenschist. The type I halo has a lower CO₂ content and is enriched in Na₂O and depleted in CaO and MnO in comparison with the greenschist. (b) Profile 2 type I blue halo vs greenschist, showing that CaO, P₂O₅, K₂O and CO₂ are enriched whereas Na₂O and SiO₂ are depleted in the type I halo. (c) Profile 1 type II blue halo vs greenschist. All major elements with the exception of K₂O plot close to the 1:1 reference line. (d) Profile 2 type II blue halo vs greenschist. All major elements plot close to the 1:1 reference line. The elemental concentrations of profile 2 are slightly different from those of profile 1. However, the metasomatic character of the type I blue halo and the more isochemical character of the type II halo, respectively, in comparison with the greenschist, can be seen even in profile 2, which is strongly affected by post-metamorphic carbonate veins.

greenschist- and blueschist-facies P - T conditions (e.g. Evans, 1990; Spear, 1993).

White mica

The compositions of white mica along the profiles are listed in Table 7 and shown graphically in Fig. 12a and b. Si (a.p.f.u.) ranges from 3.06 to 3.49 and Mg + Fe_{tot} (a.p.f.u.) ranges from 0.16 to 0.73; therefore the white mica can be classified as phengite. The phengites in type I and type II samples have generally lower $X_{\text{pyrophyllite}}$ than phengites from the greenschist in the profile, but there are no large variations in $X_{\text{paragonite}}$. Overall, the composition of phengite from the profiles is similar to that of phengite from the representative blueschist and greenschist facies (Table 6). The average Si (a.p.f.u.) of these phengites ranges from 3.4 to 3.5 and their average Mg + Fe_{tot} ranges from 0.50 to 0.51. The high Si values in phengites

from the profiles and the representative samples are most probably inherited from HP-facies conditions (Bröcker *et al.*, 1993), whereas the increase in the fraction of pyrophyllite towards the greenschist indicates a retrograde overprint at lower P (see Trotet *et al.*, 2001a; Putlitz *et al.*, 2005).

Amphibole

The compositions of amphibole along the profiles are reported in Table 7 and shown graphically in Fig. 13. Amphibole in the type I blue haloes is glaucophane. Grains become more sodic towards the rim. In the type II blue haloes near the shear zone amphibole is mostly glaucophane, whereas actinolite replaces glaucophane at its rims in these haloes further from the shear zone and in the surrounding greenschist-facies rocks. This is seen in some glaucophane grains, which have glaucophanitic

Table 6: Mineral compositions in representative blueschist-facies and greenschist-facies metabasites sampled at some distance from the shear zone

Domain:	Representative blueschist										Representative greenschist									
	Glaucophanes		Epidote		Phengite		Garnet		Calcite		Actinolite		Epidote		Phengite		Chlorite			
	08FB12	08FB12	08FB12	08FB12	08FB12	08FB12	08FB12	08FB12	24FB12	13FB12	13FB12	05FB12	05FB12	13FB12	05FB12	13FB12	05FB12			
Sample:	58-23	0-02	38-62	38-35	38-50	51-09	37-76	37-75	0-01	56-65	38-37	38-31	39-01	52-63	28-75	0-01	0-01			
Comment:	0-02	0-11	0-07	0-15	0-15	0-27	0-07	0-05	0-02	0-02	0-18	0-04	0-03	0-09	0-01	0-01	0-01			
	10-72	27-50	26-72	27-00	27-00	26-30	21-05	21-35	0-01	2-10	26-44	24-94	25-64	25-49	19-42	19-42	19-42			
	9-31	7-32	8-56	8-19	8-19	2-64	28-68	30-65	0-35	7-79	7-33	9-77	8-69	2-14	15-94	15-94	15-94			
	0-06	n.d.	n.d.	n.d.	n.d.	n.d.	0-06	0-03	0-03	0-06	0-30	0-10	0-21	0-05	0-48	0-48	0-48			
	11-08	0-08	0-05	0-10	0-10	3-47	3-03	2-86	0-76	18-74	0-13	0-05	0-08	3-93	21-98	21-98	21-98			
	0-04	n.d.	0-16	0-01	0-01	0-04	1-35	1-63	0-01	0-15	0-09	0-10	0-24	0-04	0-15	0-15	0-15			
	0-86	23-98	23-83	23-90	23-90	0-02	9-11	7-12	60-83	11-89	23-28	23-66	23-63	0-02	0-06	0-06	0-06			
	7-24	0-01	0-04	n.d.	n.d.	0-46	0-05	n.d.	0-01	0-96	n.d.	0-04	n.d.	0-32	0-01	0-01	0-01			
	0-03	0-01	0-01	0-01	0-01	10-54	n.d.	n.d.	0-01	0-09	0-01	n.d.	n.d.	10-85	0-04	0-04	0-04			
	97-60	97-63	97-79	97-85	97-85	94-83	101-16	101-44	62-04	98-44	96-13	97-00	97-53	95-57	86-83	86-83	86-83			
	7-96	3-00	2-98	2-99	2-99	3-43	5-91	5-93	<0-001	7-85	3-03	3-02	3-05	3-50	2-90	2-90	2-90			
	0-002	0-01	0-01	0-01	0-01	0-01	0-01	0-01	<0-001	0-002	0-01	0-002	0-002	0-01	0-001	0-001	0-001			
	1-73	2-52	2-45	2-47	2-47	2-08	3-89	3-95	<0-001	0-34	2-46	2-32	2-36	2-00	2-31	2-31	2-31			
	0-16	0-48	0-56	0-53	0-53	0-15	0-28	0-18	<0-001	0-13	0-48	0-64	0-57	0-12	1-35	1-35	1-35			
	0-88						3-48	3-85	0-004	0-77				0-12	1-35	1-35	1-35			
	0-01						0-01	0-004	<0-001	0-01	0-02	0-01	0-01	0-003	0-04	0-04	0-04			
	2-26	0-01	0-01	0-01	0-01	0-35	0-71	0-67	0-02	3-87	0-02	0-01	0-01	0-39	3-31	3-31	3-31			
	0-01	n.d.	0-01	<0-001	<0-001	0-002	0-18	0-22	<0-001	0-02	0-01	0-01	0-02	0-002	0-01	0-01	0-01			
	0-13	1-99	1-99	1-99	1-99	0-002	1-53	1-20	0-98	1-77	1-97	2-00	1-98	0-002	0-01	0-01	0-01			
	1-92	0-002	0-01	0-01	0-01	0-06	0-01	0-01	<0-001	0-26	0-01	0-01	0-01	0-04	0-001	0-001	0-001			
	0-01					0-90	0-90	16-00	<0-001	0-02	0-001	8-01	8-00	0-92	0-01	0-01	0-01			
	15-05	8-00	8-01	8-00	8-00	6-99	16-00	16-00	1-00	15-04	8-00	8-01	8-00	6-98	9-93	9-93	9-93			
	0-72	0-52	0-45	0-47	0-47	0-70	0-17	0-15	0-83	0-83	0-48	0-33	0-38	0-77	0-71	0-71	0-71			
							0-59	0-65												
							0-12	0-11												
							0-03	0-04												
							0-19	0-16												

$X_{Mg} = Mg / (Mg + Fe^{2+})$. Ferric iron of glaucophane is calculated on the basis of 23 oxygens with Fe^{2+} / Fe^{3+} estimation assuming 13 cations (after Leake *et al.*, 1997). Ferric iron of garnet is calculated on the basis of 12 oxygens.

Table 7: Compositions of minerals from the type I and type II blue haloes and the greenschist

Domain:	Type I blue halo										
Mineral:	Glaucophane			Epidote			Phengite			Chlorite	
Sample:	0.05-1FB			0.1-2FB			0.05-1FB			0.05-1FB	
Comment:	core	rim 1	rim 2								
SiO ₂	58.05	58.13	58.06				38.40		50.59		28.31
TiO ₂	0.03	0.07	n.d.				0.09		0.21		n.d.
Al ₂ O ₃	11.52	10.53	9.95				26.92		29.57		20.36
FeO(tot)	7.38	9.79	11.95				7.81		1.57		18.47
Cr ₂ O ₃	0.07	0.06	0.06				0.02		0.06		0.09
MgO	12.35	11.09	10.14				0.03		3.62		20.75
MnO	0.04	0.20	0.13				0.02		0.03		0.35
CaO	1.83	0.56	0.33				23.24		n.d.		0.04
Na ₂ O	6.62	6.97	7.23				0.04		0.62		n.d.
K ₂ O	0.04	0.02	0.04				0.02		9.41		0.04
Total	97.93	97.42	97.89				96.58		95.68		88.40
Si	7.83	7.91	7.94				3.01		3.33		2.84
Ti	0.003	0.01					0.01		0.01		
Al	1.83	1.69	1.60				2.49		2.29		2.46
Fe ³⁺	0.22	0.46	0.49				0.51				
Fe ²⁺	0.62	0.65	0.88						0.09		1.55
Cr	0.01	0.01	0.01				0.001		0.003		0.01
Mg	2.48	2.25	2.07				0.003		0.36		3.11
Mn	0.005	0.02	0.02				0.001		0.002		0.03
Ca	0.26	0.08	0.05				1.95				0.004
Na	1.73	1.84	1.92				0.01		0.08		
K	0.01	0.004	0.01				0.002		0.79		0.01
Total	15.00	14.92	14.97				7.98		6.95		10.00
X _{Mg}	0.80	0.78	0.70						0.80		0.67
X _{Cz}							0.49				
X _{Alm}											
X _{Pyr}											
X _{Sps}											
X _{Grs}											

Domain:	Type II blue halo										
Mineral:	Glaucophane			Actinolite		Epidote			Carbonates		
Sample:	0.5-1FB			0.5-1FB		0.25-2FB			0.25-2FB		
Comment:	core	rim 1	rim 2	core	rim 1	rim 2	core	rim 1	rim 2	calcite	dolomite
SiO ₂	58.16	57.45	58.06	58.30	55.38	55.66	39.08	38.21	38.35	0.08	0.15
TiO ₂	0.003	0.01	0.06	0.02	n.d.	n.d.	0.17	0.02	0.05	n.d.	n.d.
Al ₂ O ₃	11.75	10.17	10.29	10.92	2.16	1.56	28.48	25.37	24.79	0.06	0.03
FeO(tot)	6.70	9.76	9.05	9.37	9.47	9.12	5.41	9.22	9.92	0.37	0.65
Cr ₂ O ₃	0.09	0.01	0.06	0.01	0.02	0.05	0.03	0.03	0.01	n.d.	n.d.
MgO	12.27	11.31	11.70	10.88	17.54	17.84	0.09	n.d.	n.d.	1.19	18.99

(continued)

Table 7: Continued

Domain:	Type II blue halo										
Mineral:	Glaucofane			Glaucofane	Actinolite	Actinolite	Epidote			Carbonates	
Sample:	0.5-1FB			0.5-1FB	0.5-1FB	0.5-1FB	0.25-2FB			0.25-2FB	
Comment:	core	rim 1	rim 2	core	rim 1	rim 2	core	rim 1	rim 2	calcite	dolomite
MnO	0.04	0.19	0.21	0.14	0.35	0.23	0.03	0.30	0.28	0.03	0.28
CaO	1.20	1.20	0.69	0.43	10.92	10.62	23.94	23.66	23.26	58.95	37.42
Na ₂ O	6.58	6.59	6.82	6.97	1.49	1.44	0.09	0.36	0.04	0.01	0.06
K ₂ O	0.05	0.03	0.02	0.08	0.11	0.08	n.d.	0.20	0.03	0.03	0.08
Total	96.85	96.72	96.97	97.12	97.44	96.60	97.32	97.37	96.73	60.71	57.65
Si	7.87	7.89	7.91	7.95	7.80	7.87	3.03	3.00	3.03	0.001	0.002
Ti	<0.001	0.001	0.01	0.002			0.01	0.001	0.003		
Al	1.87	1.65	1.65	1.75	0.36	0.26	2.60	2.35	2.31	0.001	<0.001
Fe ³⁺	0.28	0.45	0.51	0.37	0.32	0.37	0.35	0.61	0.66		
Fe ²⁺	0.48	0.67	0.52	0.70	0.80	0.71				0.00	0.01
Cr	0.01	0.001	0.01	0.001	0.002	0.01	0.00	0.00	0.00		
Mg	2.48	2.32	2.38	2.21	3.68	3.76	0.01	0.00	0.00	0.03	0.41
Mn	0.01	0.02	0.02	0.02	0.04	0.03	0.00	0.02	0.02	<0.001	0.003
Ca	0.17	0.18	0.10	0.06	1.65	1.61	1.99	1.99	1.97	0.96	0.58
Na	1.73	1.76	1.80	1.84	0.41	0.39	0.01	0.05	0.01	<0.001	0.002
K	0.01	0.01	0.004	0.01	0.02	0.01		0.02	0.00	0.001	0.001
Total	14.91	14.94	14.91	14.92	15.08	15.02	8.00	8.05	7.99	1.00	1.00
X _{Mg}	0.84	0.78	0.82	0.76	0.82	0.84					
X _{cz}							0.63	0.37	0.32		
X _{Alm}											
X _{Pyr}											
X _{Sps}											
X _{Grs}											

Domain:	Type II blue halo				Greenschist						
Mineral:	Phengite	Chlorite	Garnet		Glaucofane	Actinolite	Epidote		Phengite	Chlorite	
Sample:	0.5-1FB	0.25-2FB	0.25-2FB		1.2-1FB	1.2-1FB	0.4-2FB		1.2-1FB	0.4-2FB	
Comment:			core	rim	core	rim 1	core	rim 1	rim 2		
SiO ₂	51.74	28.10	38.00	38.21	55.11	57.26	39.14	38.60	38.19	51.41	28.58
TiO ₂	0.04	0.06	0.09	0.14	0.09	0.03	0.13	0.10	0.12	0.25	0.04
Al ₂ O ₃	27.06	20.20	20.89	20.83	6.12	1.03	29.01	27.48	25.53	29.41	19.69
FeO(tot)	1.77	21.43	25.06	27.45	7.42	8.52	4.95	6.42	9.17	1.67	19.96
Cr ₂ O ₃	0.09	0.01	0.03	0.01	0.07	0.03	0.01	0.12	0.01	0.10	0.06
MgO	3.92	18.81	1.48	1.86	17.17	18.28	n.d.	0.01	n.d.	3.52	20.47
MnO	0.03	0.52	6.85	4.69	0.11	0.36	0.03	0.14	0.31	0.03	0.22
CaO	0.07	n.d.	7.66	7.94	9.61	12.05	24.35	23.80	23.57	n.d.	0.11
Na ₂ O	0.46	0.01	0.03	0.06	2.49	0.69	0.04	0.03	0.10	0.40	0.08
K ₂ O	10.35	0.03	0.02	0.02	0.10	0.07	0.03	0.01	0.08	9.58	0.01
Total	95.52	89.18	100.11	101.21	98.29	98.32	97.68	96.70	97.07	96.36	89.21
Si	3.43	2.84	6.08	6.04	7.59	7.99	3.02	3.02	3.00	3.36	2.86

(continued)

Table 7: Continued

Domain:	Type II blue halo				Greenschist						
	Phengite	Chlorite	Garnet		Glauco-phane	Actinolite	Epidote			Phengite	Chlorite
Sample:	0.5-1FB	0.25-2FB	0.25-2FB		1.2-1FB	1.2-1FB	0.4-2FB			1.2-1FB	0.4-2FB
Comment:			core	rim	core	rim 1	core	rim 1	rim 2		
Ti	0.00	0.01	0.01	0.02	0.01	0.003	0.01	0.01	0.01	0.01	0.003
Al	2.11	2.47	3.94	3.88	0.99	0.17	2.64	2.53	2.37	2.26	2.38
Fe ³⁺				0.03	0.27	0.05	0.32	0.42	0.60		
Fe ²⁺	0.10	1.81	3.36	3.60	0.58	0.95				0.09	1.67
Cr	0.01	0.00	0.004	0.002	0.01	0.003	0.001	0.01	<0.001	0.01	0.01
Mg	0.39	2.84	0.35	0.44	3.53	3.80		0.001		0.34	3.06
Mn	0.00	0.05	0.93	0.63	0.01	0.04	0.002	0.01	0.02	0.001	0.02
Ca	0.01		1.31	1.35	1.42	1.80	2.01	1.99	1.99		0.01
Na	0.06	0.003	0.01	0.02	0.67	0.19	0.01	0.00	0.01	0.05	0.02
K	0.88	0.004	0.01	0.01	0.02	0.01	0.003	0.001	0.01	0.80	0.001
Total	6.98	10.01	16.00	16.00	15.10	15.00	8.00	8.00	8.01	6.92	10.03
X _{Mg}	0.80	0.61	0.09	0.11	0.86	0.80				0.79	0.65
X _{Cz}							0.67	0.56	0.38		
X _{Alm}			0.56	0.60							
X _{Pyr}			0.06	0.07							
X _{Sps}			0.16	0.10							
X _{Grs}			0.22	0.22							

$X_{Mg} = Mg / (Mg + Fe^{2+})$. Ferric iron of glaucophane is calculated on the basis of 23 oxygens with Fe²⁺/Fe³⁺ estimation assuming 13 cations (after Leake *et al.*, 1997). Ferric iron of garnet is calculated on the basis of 12 oxygens.

(Na- and Al-enriched) cores and actinolitic (Ca-, Fe- and Mg-enriched) rims (Table 7 and Fig. 7). The chemical composition of glaucophane from the type I and type II haloes is similar to that of glaucophane from the representative blueschist-facies rocks (Table 6). The composition of actinolite does not show any major difference between mineral grains from the profile and from the surrounding representative greenschist-facies metabasites (Table 6).

Garnet

Garnet is partly replaced by chlorite in both types of blue halo and in the surrounding greenschist-facies rocks. Garnets are mostly almandine with slight core-to-rim Mg and Fe enrichment and Mn depletion (Table 7). The composition and zoning pattern of the garnets from the profiles is consistent with those observed in representative blueschist-facies metabasites (Table 6).

Carbonates

Carbonates that occur within the matrix and replacing HP minerals are usually pure calcite, whereas those growing

as filling material within late-stage veins are of a more dolomitic composition (Tables 6 and 7).

In summary, we did not find systematic variation in the compositions of epidote, chlorite and albite. However, we found that glaucophane crystals in the type I blue halo had sodic rims, which is consistent with metasomatic addition of Na, whereas glaucophane crystals in the type II blue halo had actinolitic rims, consistent with a greenschist-facies overprint of a blueschist-facies rock. Additionally, the chemical compositions of phengite and garnet confirm that these minerals were most probably formed at HP–LT conditions.

METAMORPHIC TIMELINE

Based on modal, textural and chemical data we constructed a metamorphic timeline for our study area. This is shown graphically in Fig. 14 and outlined below.

- (1) Metamorphism occurred at blueschist-facies conditions producing the assemblage glaucophane + epidote + garnet + phengitic mica.

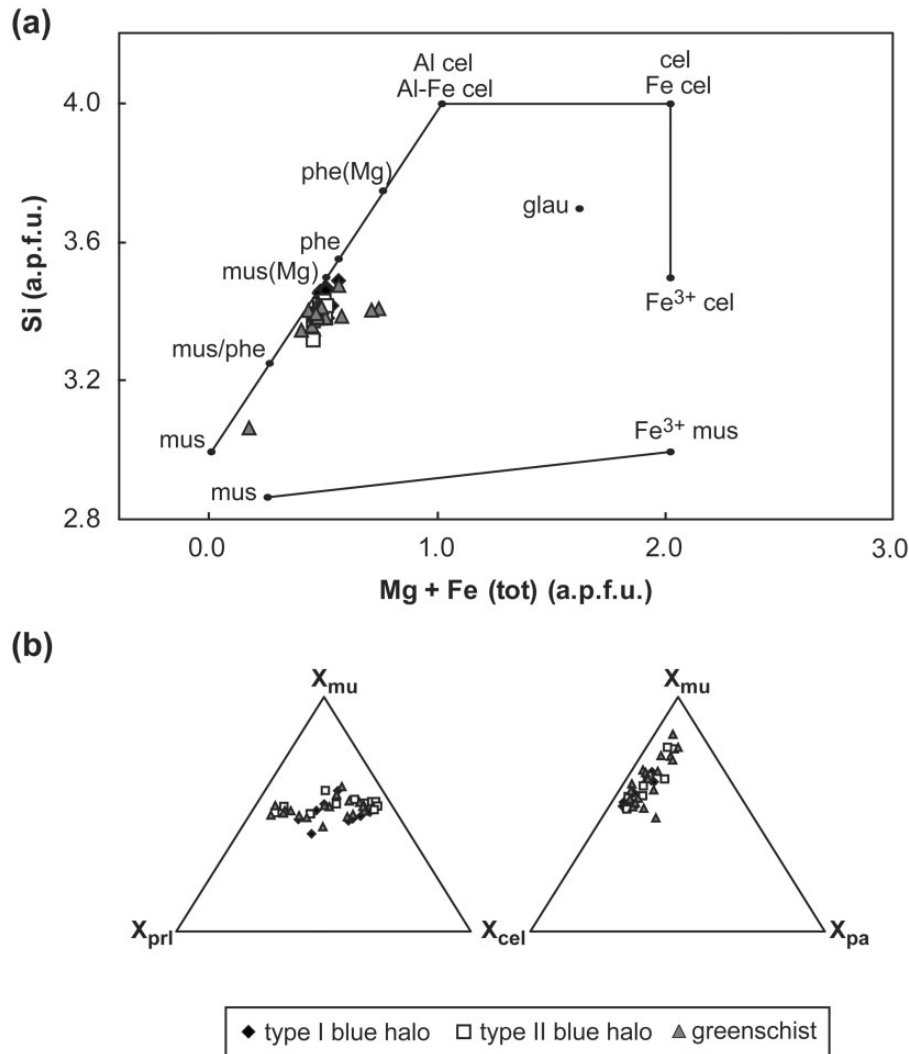


Fig. 12. (a) Classification of the white mica from the profiles in terms of Si vs Mg + Fe a.p.f.u. (after Tischendorf *et al.*, 2004). Most of the white micas are similar to muscovite and phengite. (b) Ternary diagrams showing the white mica compositions in terms of the endmembers muscovite (X_{mu}), celadonite (X_{cel}), paragonite (X_{pa}) and pyrophyllite (X_{prl}).

- (2) Foliation development was accompanied by carbonation, causing replacement of glaucophane and epidote by calcite (Fig. 6c and d). This is seen in the type II blue halo. Because carbonation in the type II blue halo is more extensive closer to the shear zone we infer that the shear zone provided a conduit for the CO₂-bearing fluids that caused carbonation.
- (3) Metasomatism occurred at blueschist-facies conditions, causing breakdown of epidote and replacement of phengite by glaucophane, gain of SiO₂ and Na₂O, and loss of K₂O, Al₂O₃, CaO, MnO and CO₂. This is seen in the type I blue halo. The relative timing of metasomatism and carbonation remains uncertain.
- (4) Retrograde decarbonation occurred at greenschist-facies conditions, causing replacement of glaucophane, epidote, garnet, phengitic mica and calcite by

chlorite and albite (Fig. 8). This is seen in the type II blue halo and surrounding greenschist-facies rocks. Based on sigmoidal inclusion trails in retrograde albite porphyroblasts, we infer that retrogression occurred towards the end of the time during which the foliation was developing.

In the following sections, we consider the type I and II blue haloes in the framework of this timeline.

Type I blue halo

The type I blue halo is composed of glaucophane schist. We interpret that this rock was formed by metasomatism caused by fluids flowing along the shear zone at

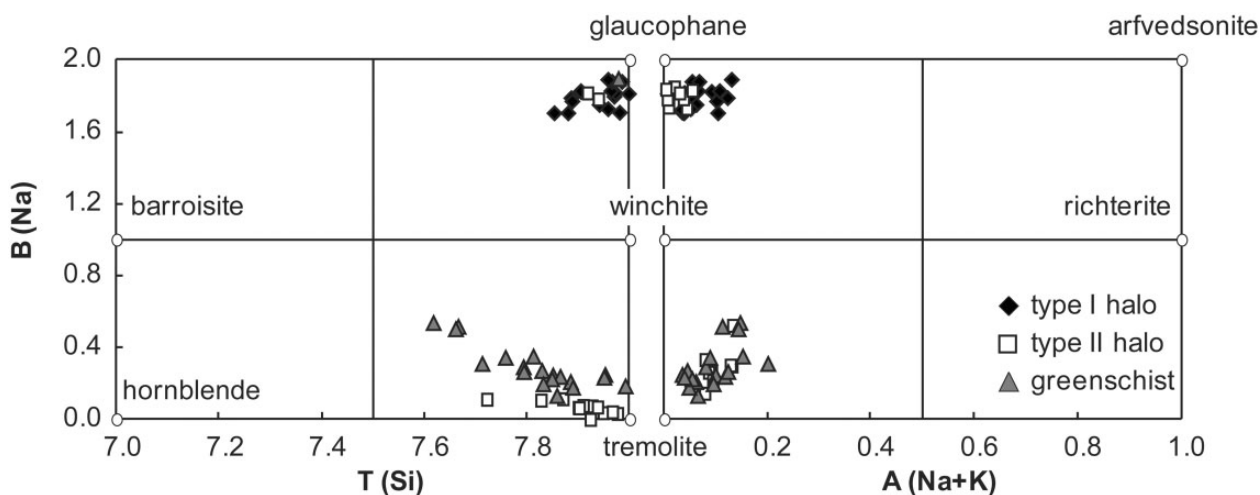


Fig. 13. Classification of the amphiboles from the two types of blue halo and the greenschist (after Leake *et al.*, 1997). The dominant amphibole in the two types of halo is glaucophane. The dominant amphibole in the greenschist is tremolite–actinolite.

blueschist-facies conditions. This interpretation is based on the following evidence.

- (1) Concentrations of Na, Si, Fe and the HFSE increase towards the shear zone and concentrations of Ca, Sr, Al, Mn, some of the REE and CO₂ decrease towards the shear zone within the type I halo. Thus, concentrations of both mobile and immobile elements vary within the type I halo.
- (2) The modal amount of glaucophane increases by 30–40% and the modal amounts of phengite, chlorite and calcite decrease towards the shear zone within the type I halo.
- (3) Glaucophane replaces phengite in the type I halo; this is consistent with the increase of Na and Si concentrations and decrease of Al concentration towards the shear zone. Loss in Ca is indicated in the breakdown of epidote.
- (4) Glaucophane rims are sodic in the type I halo, which is consistent with the increase of Na concentration towards the shear zone.

Type II blue halo

The type II blue halo is composed of carbonated blueschist-facies metabasite that has been variably retrogressed at greenschist-facies conditions. The least retrogressed blueschist-facies rocks are found closest to the shear zone. The extent of greenschist-facies retrogression increases with distance from the shear zone. We interpret that carbonated blueschist-facies rocks, similar to those observed elsewhere in the Cyclades (e.g. Schliestedt & Matthews, 1987; Bröcker, 1990; Miller *et al.*, 2009) were preserved in the type II halo by fluids flowing along the shear zone at

greenschist-facies conditions. This interpretation is based on the following evidence.

- (1) Both modal data and reaction textures from the type II blue halo unequivocally show that blueschist-facies minerals were replaced by greenschist-facies minerals. There is no evidence of new growth of blueschist-facies minerals that would have been expected if the blueschist has been formed by metasomatism.
- (2) Glaucophane rims are actinolitic in the type II blue halo. The Mn content in garnet decreases from core to rim, which indicates garnet growth during prograde metamorphism. High Si values and high fractions of pyrophyllite in phengites imply that the phengite derives from an HP regime but was overprinted during retrogression at lower *P*.
- (3) There is little evidence of the chemical mobility that would have been expected if the blueschist has been formed by metasomatism. The only elements that show variability within the type II halo are K and the LILE. These elements are mobile and although variability of their concentrations could be inherited from the protolith a more probable cause is fluid-induced mobility. Mobilization of the LILE on Syros has also been reported by Breeding *et al.* (2004). However, mobility of K and the LILE cannot account for the observed mineralogical differences between blueschist- and greenschist-facies rocks.

This interpretation is enigmatic because retrogression is usually more extensive along fluid pathways (e.g. shear zones) than in more ‘dry’ areas far away from these fluid pathways (e.g. Ring *et al.*, 2010). On the other hand, Gao & Klemd (2001) and Beinlich *et al.* (2010) have reported eclogite veins in blueschist-facies rocks from Tianshan,

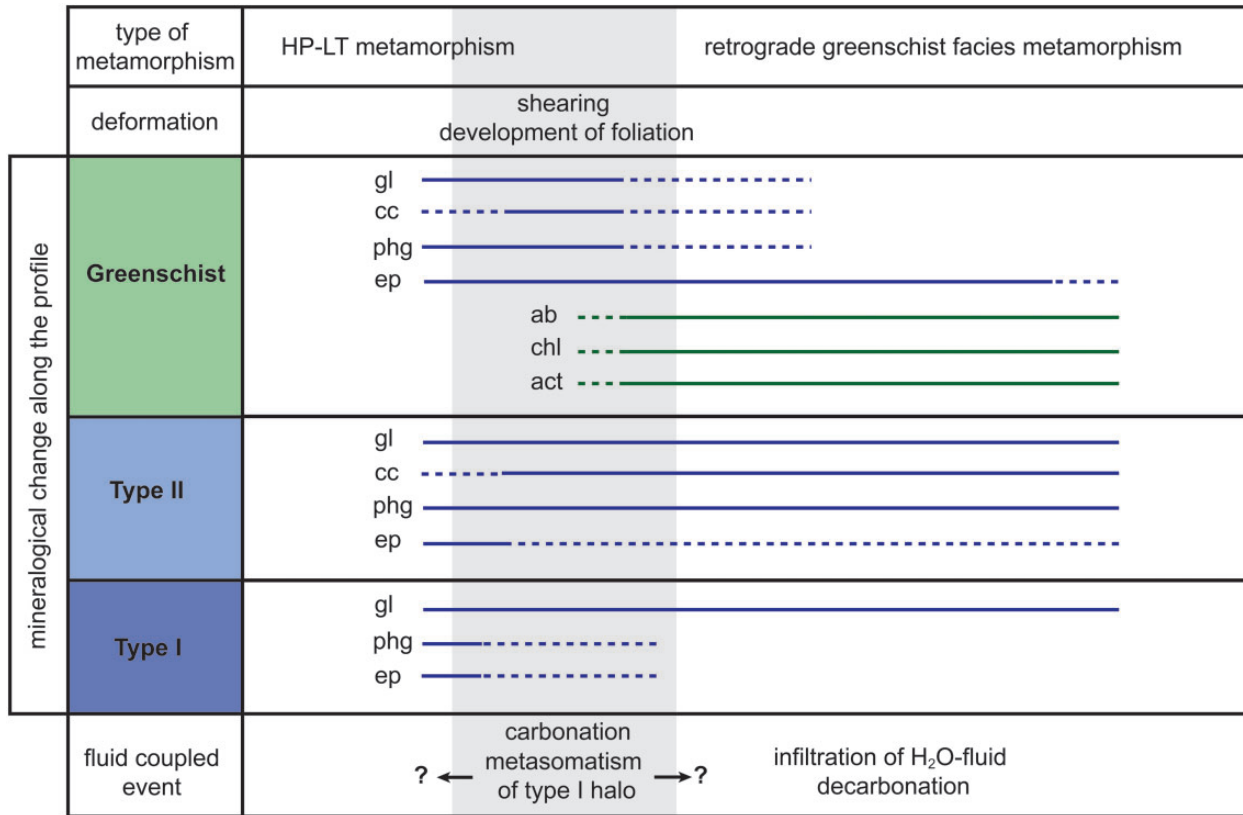


Fig. 14. Schematic illustration of the appearance and breakdown of key minerals during the various fluid infiltration and metamorphic events. Carbonation of the HP-LT mineral assemblages started most probably very early and can be attributed to more or less pervasive flow of a CO₂-bearing fluid. The shear zone was most probably already a fluid pathway before greenschist-facies metamorphism, as carbonation appears to be more extensive along the shear zone. During retrogression, decarbonation led to the release of CO₂. Metasomatism of the type I blue halo most probably occurred before or at the same time as the rock became foliated. However, the possibility cannot be excluded that metasomatism occurred later and that the newly formed glaucophane crystals mimic a pre-existing foliation.

NW China. They present compelling evidence that these veins were formed by prograde dehydration. Below we propose a model whereby blueschist-facies minerals were preserved during retrograde decarbonation (rather than formed by prograde dehydration).

BLUESCHIST PRESERVATION

In our model, we propose that blueschist was preserved in the type II halo by fast-flowing CO₂-bearing fluids along the shear zone. To illustrate this model, we begin by constructing a simplified P - T vs X_{CO_2} pseudosection. The purpose of this pseudosection is to show how blueschist-facies minerals might have been preserved in a simple system at greenschist-facies conditions if X_{CO_2} had been elevated.

P - T vs X_{CO_2} pseudosection

We used PerPlex version 6.6.6 (Connolly, 1990, 2005, 2009) to construct a set of T - X_{CO_2} pseudosections at pressures ranging from 0.6 to 1.0 GPa in the system NCFMASH +

CO₂ with SiO₂ in excess (Fig. 15). Solid solution models were considered for chlorite (Holland *et al.*, 1998), garnet (Holland & Powell, 1998), amphiboles (Dale *et al.*, 2005) and carbonates (Holland & Powell, 2003).

The bulk-rock composition we used to calculate our pseudosection was the average of samples 0.5-1FB to 1.2-1FB from profile 1 (Table 8). These samples were least affected by metasomatism and the average bulk composition is similar to that of the representative samples of greenschist- and blueschist-facies rocks. Total iron was treated as FeO and all K₂O was treated as Na₂O. These simplifications allowed us to work in a system that was both computationally manageable and able to reproduce the observed mineral assemblages.

One of the shortcomings of working in this simplified system is that phengite needs to be represented by paragonite. This is in part justified because replacement of phengite by glaucophane (see Fig. 6a) could imply that the phengite was originally paragonitic. Glaucophane and epidote stabilities are probably reduced because these minerals are stabilized by Fe₂O₃ (Owen, 1989; Diener &

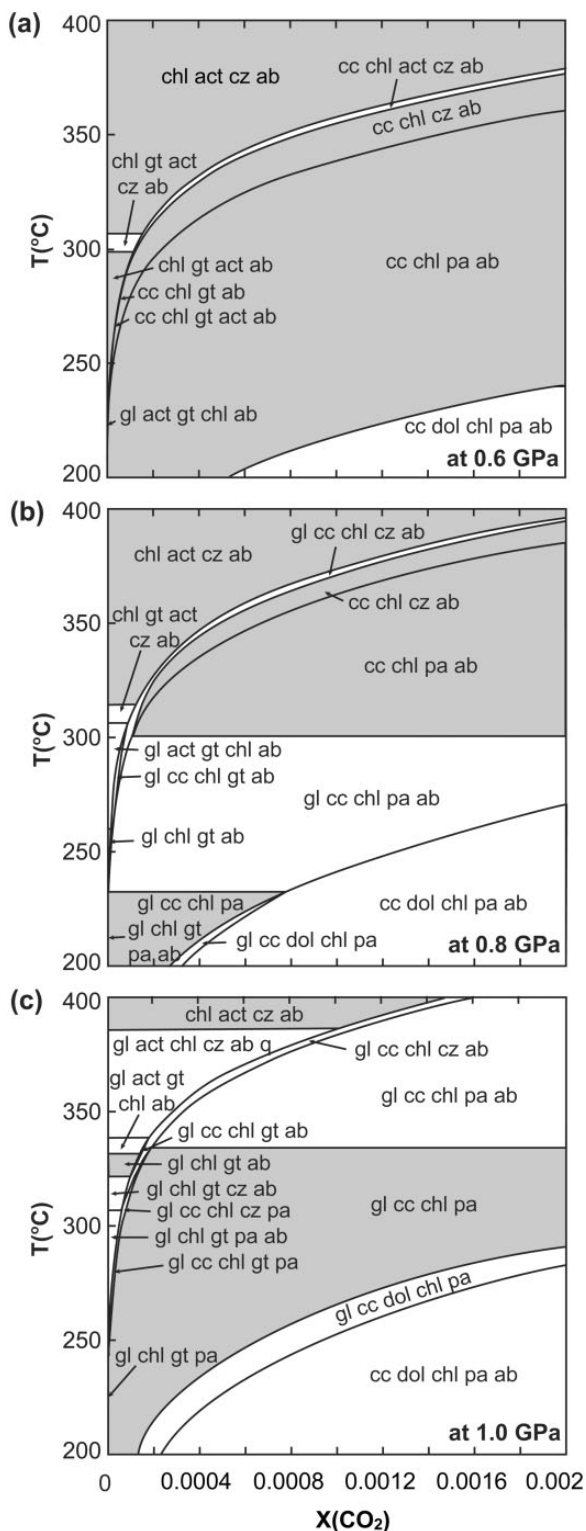


Fig. 15. $T-X_{CO_2}$ pseudosections calculated in the NCFMASH + CO_2 system at pressures of (a) 0.6 GPa, (b) 0.8 GPa and (c) 1.0 GPa with SiO_2 in excess. ab, albite; act, actinolite; cc, calcite; chl, chlorite; cz, clinozoisite; gl, glaucophane; gt, garnet (grossular); pa, paragonite.

Table 8: Bulk composition (in mol %) used for the construction of the $T-X_{CO_2}$ pseudosections (Fig. 15) and $P-T$ vs X_{CO_2} diagrams (Fig. 16)

	Bulk composition (mol %)
SiO_2	in excess
Al_2O_3	10.36
FeO	6.69
MgO	14.91
CaO	10.40
$Na_2O + K_2O$	4.54

The bulk composition is calculated based on the average compositions of the last four samples from profile 1, which are assumed to be least affected by fluid flow through the shear zone.

Powell, 2010). However, we consider that the simplified system suffices for our purposes, which are largely illustrative.

The pseudosections were constructed for the minerals glaucophane, actinolite, paragonite, clinozoisite, chlorite, albite, quartz and calcite in the system NCFMASH + CO_2 . We then used PerPlex to construct a set of $P-T$ vs X_{CO_2} pseudosections for three thermal gradients: $300^\circ C\ GPa^{-1}$, $350^\circ C\ GPa^{-1}$ and $400^\circ C\ GPa^{-1}$ (Fig. 16). These gradients were chosen to reflect the range from greenschist-facies to blueschist-facies conditions and are based on the $P-T$ paths of Trotet *et al.* (2001a), Keiter *et al.* (2004) and Schumacher *et al.* (2008a).

The $P-T$ vs X_{CO_2} pseudosections show that a carbonated blueschist-facies assemblage containing glaucophane + paragonite + calcite is stable at higher X_{CO_2} , whereas a greenschist-facies assemblage containing albite + chlorite + actinolite or albite + chlorite + clinozoisite is stable at lower X_{CO_2} in the system NCFMASH + CO_2 at the transition between blueschist- and greenschist-facies conditions (Fig. 16). Cooler thermal gradients result in the expansion of the blueschist-facies stability fields whereas warmer gradients lead to an extension of the greenschist-facies stability fields towards higher P and T .

The $P-T$ vs X_{CO_2} pseudosections in Fig. 16 were calculated for phases with unit activities. As mentioned above, the use of paragonite instead of phengite in our thermodynamic modelling is a major shortcoming. Therefore, mineral activities for paragonite were calculated with appropriate $A-X$ relations at different pressures and temperatures using the actual mineral compositions to test the effect of lower activities of paragonite on the system. Using these calculated activities in the calculations of the pseudosections results in the extension of the

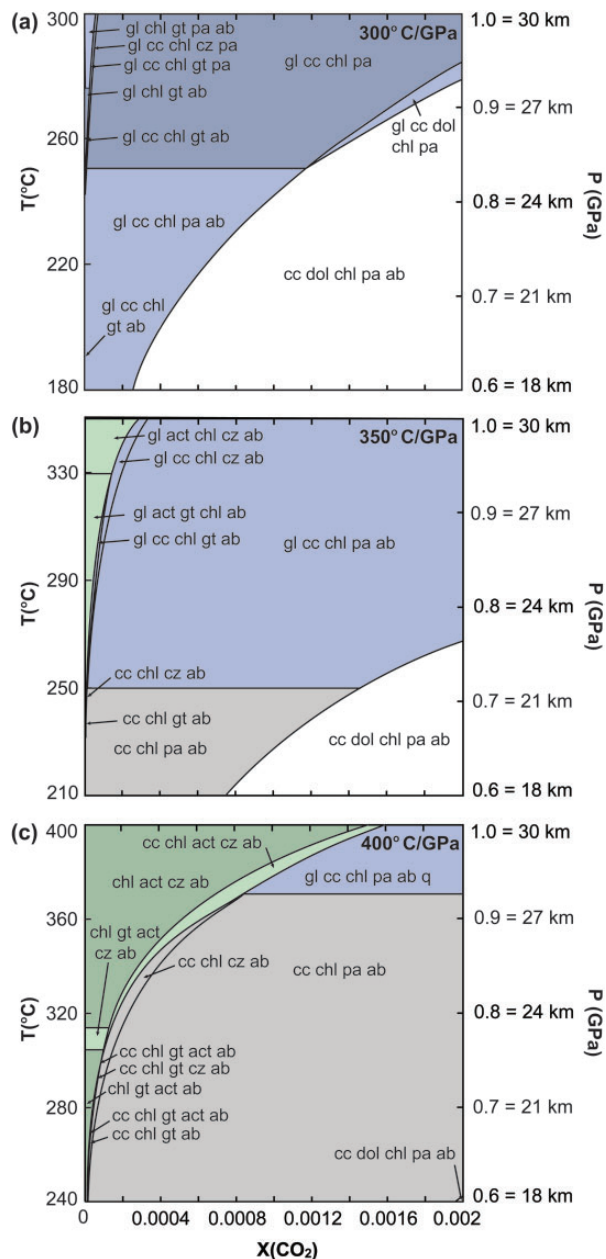


Fig. 16. P – T vs X_{CO_2} diagrams for three thermal gradients (a) $300^\circ\text{C GPa}^{-1}$, (b) $350^\circ\text{C GPa}^{-1}$ and (c) $400^\circ\text{C GPa}^{-1}$. Glaucophane is stabilized at low T and P by an increase of X_{CO_2} . Stability fields containing glaucophane are coloured blue and are assumed to represent blueschist-facies mineral assemblages; stability fields containing actinolite \pm glaucophane are coloured green and are assumed to represent greenschist-facies mineral assemblages. ab, albite; act, actinolite; cc, calcite; chl, chlorite; cz, clinozoisite; gl, glaucophane; gt, garnet (grossular); pa, paragonite.

glaucophane- and albite-bearing stability fields towards lower pressures and lower temperatures.

We note that reactions predicted using the simple system NCFMASH + CO_2 are actually very similar to those that can be deduced from modal and textural data (Figs 4–9).

The modes of the blueschist-facies minerals glaucophane, paragonite and calcite decrease towards lower X_{CO_2} in the same way as the modes of the greenschist-facies minerals actinolite, albite and chlorite increase. However, very low X_{CO_2} conditions in the P – T vs X_{CO_2} pseudosection (e.g. 0.0–0.0001 for the thermal gradient $350^\circ\text{C GPa}^{-1}$) can be ruled out as they predict the formation of the Ca-bearing garnet grossular, which is not supported by our data. The formation of grossular probably arises because Ca released from the breakdown of calcite is incorporated into the structure of the garnet instead of into Ca-bearing amphibole.

In the following section, we use the P – T vs X_{CO_2} pseudosections to illustrate how blueschist-facies minerals could have been preserved alongside the shear zone if X_{CO_2} had been elevated by fluid flowing along this shear zone.

Preservation of blueschist-facies minerals in the type II haloes

In our model (Fig. 17), a carbonated blueschist-facies assemblage was preserved in the type II blue haloes during greenschist-facies hydration because X_{CO_2} was elevated by CO_2 diffusing outwards from the shear zone. Our model assumes that (1) fluid flow along the shear zone was faster than in the surrounding rocks and (2) fluid flowing along the shear zone had higher X_{CO_2} than fluid flowing through the surrounding rocks at greenschist-facies conditions.

Our first assumption is supported by studies that show that metamorphic fluids are channeled along shear zones (e.g. Zack & John, 2007, and references therein) and studies that show that extensive quartz veining requires high fluid fluxes (e.g. Ague, 2011, and references therein).

Our second assumption requires a source of CO_2 -bearing fluid that was tapped by the shear zone. Based on mineral equilibria in glaucophane marbles, Schumacher *et al.* (2008b) argued that the X_{CO_2} of the metamorphic fluid on Syros was typically ~ 0.01 . This is sufficient to stabilize a carbonated blueschist-facies mineral assemblage at greenschist-facies conditions in our simplified chemical system (Fig. 18).

Interestingly, because of the positive slope of decarbonation reaction curves on the P – T vs X_{CO_2} pseudosections shown in Fig. 16 and represented schematically in Fig. 18, the X_{CO_2} of a fluid buffered by a given decarbonation reaction at higher P – T conditions could inhibit decarbonation occurring at lower P – T conditions (Fig. 18) if fluid flow along the shear zone was fast relative to the rate of decarbonation within the surrounding rocks. This could occur as described below.

Let us consider decarbonation of a carbonated blueschist-facies assemblage at greenschist-facies conditions caused by reaction with a hydrous fluid that we assume to flow pervasively upwards. Pervasive decarbonation caused by this hydrous fluid is represented by the blue arrow in

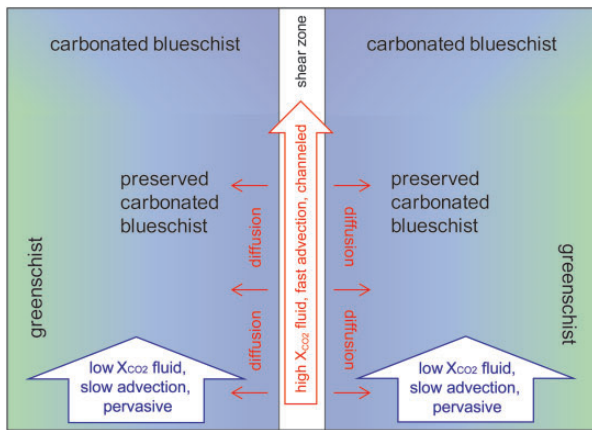


Fig. 17. Model for localized blueschist preservation along the shear zone. A carbonated blueschist-facies assemblage was preserved in the type II blue haloes during greenschist-facies hydration because X_{CO_2} was elevated by CO_2 diffusing outwards from the shear zone.

Fig. 18. The X_{CO_2} of the fluid upstream of (i.e. structurally below) the reaction front is zero (for a pure H_2O fluid), whereas the X_{CO_2} of fluid downstream of (i.e. structurally above) the reaction front is buffered by the decarbonation reaction (Fig. 18). The fluid composition downstream of the reaction front is therefore fixed by the reaction curve that is highlighted in Fig. 18. It is likely that the reaction front will experience diffusive and/or kinetic broadening and the reaction will therefore occur simultaneously over some range of P - T conditions (Fig. 18). This range of P - T conditions (or depths) is represented by the width of the blue arrow in Fig. 18. The X_{CO_2} of the fluid downstream of the reaction front would continue to be buffered by the reaction and would therefore range from $X_{\text{CO}_2,2}$ to $X_{\text{CO}_2,1}$ provided that fluid flow was pervasive and slow relative to the rate of the decarbonation reaction. If fluid flow became channeled (e.g. by a shear zone) an interesting situation arises (Fig. 18), as follows.

- (1) Fluid flow within the rocks surrounding the shear zone remains slow relative to the reaction rate and the X_{CO_2} of this fluid continues to be buffered by the reaction and therefore ranges from $X_{\text{CO}_2,2}$ to $X_{\text{CO}_2,1}$. This is shown by the black arrow in Fig. 18.
- (2) Fluid flow along the shear zone would be faster. If fluid flow was sufficiently fast compared with the rate of the decarbonation reaction, X_{CO_2} would no longer be effectively buffered by this reaction and would remain close to $X_{\text{CO}_2,2}$. This is shown by the red arrow in Fig. 18.

The consequence of this situation would be that the X_{CO_2} of the fluid flowing along the shear zone would become progressively higher than the X_{CO_2} of the fluid flowing within the surrounding rocks. Expressed another way, the X_{CO_2} of the fluid flowing along the shear zone

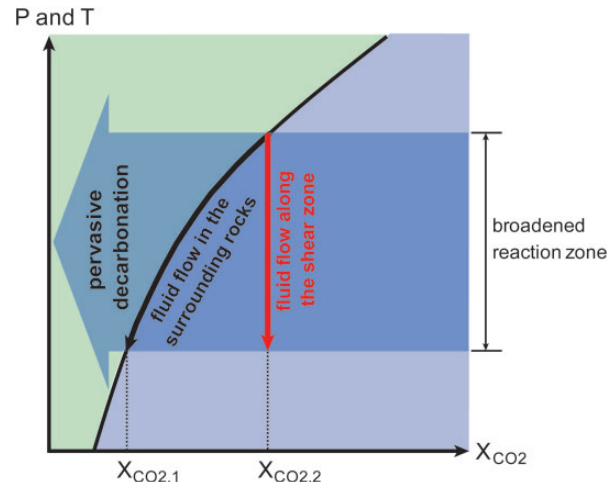


Fig. 18. Simplified sketch of a P - T vs X_{CO_2} diagram based on Fig. 16. Pervasive decarbonation was caused by a hydrous fluid. The reaction front most probably experienced diffusive and/or kinetic broadening and the reaction will therefore occur simultaneously over some range of P - T conditions (blue arrow). The X_{CO_2} of the fluid upstream of the reaction front is zero (for a pure H_2O fluid), whereas the X_{CO_2} of the fluid downstream of the reaction front is buffered by the decarbonation reaction and fixed to the reaction curve (black arrow). In the case of channelization of fluid flow along a shear zone fluid flow within the surrounding rocks remains slow relative to the reaction rate and the X_{CO_2} of this fluid continues to be buffered by the reaction and therefore ranges from $X_{\text{CO}_2,2}$ to $X_{\text{CO}_2,1}$ (black arrow). If fluid flow within the shear zone is sufficiently fast, X_{CO_2} is no longer effectively buffered by the decarbonation reaction and remains close to $X_{\text{CO}_2,2}$ (red arrow). The X_{CO_2} of the fluid flowing along the shear zone becomes progressively higher than the X_{CO_2} of the fluid flowing within the surrounding rocks. This inhibits progress of the decarbonation reaction, causing the carbonated blueschist-facies assemblage to be preserved close to the shear zone.

would become elevated with respect to the reaction curve. This would inhibit progress of the decarbonation reaction, causing the carbonated blueschist-facies assemblage to be preserved close to the shear zone. This is the type II blue halo.

It is important to note that this model can explain only local preservation of blueschist-facies rocks, specifically alongside a shear zone or other high flux pathway and within a broadened reaction zone. This model cannot explain widespread preservation of blueschist-facies rocks.

Fluid flux along the shear zone

The P - T vs X_{CO_2} pseudosections (Fig. 16) can be used for the calculation of fluid fluxes in the shear zone. We can estimate the fluid flux along the shear zone from the width of the type II blue halo.

If CO_2 diffusion outwards from the shear zone controls the width of the type II blue halo (x^*), we can write the following equation, which is based on the solution to Fick's Law in one dimension:

$$X_{\text{CO}_2,1} = X_{\text{CO}_2,2} \cdot \text{erfc} \left(\frac{x^*}{2\sqrt{D\phi\tau t}} \right) \quad (1)$$

where $X_{\text{CO}_2,1}$ represents X_{CO_2} of fluid buffered by the reaction (Fig. 18), $X_{\text{CO}_2,2}$ represents the X_{CO_2} of fluid within the shear zone (Fig. 18), D is CO_2 diffusivity in the fluid, ϕ is porosity, τ is tortuosity and t is time. It should be noted that the fluid composition at x^* (corresponding to the width of the type II blue halo and the position of the 'preservation front') is in equilibrium with both reactants and products of greenschist-facies hydration, and for this reason $X_{\text{CO}_2} = X_{\text{CO}_2,1}$ at x^* .

We can also write two equations for the vertical distance by which fluid flowing upwards along the shear zone advances ahead of fluid flowing upwards within the surrounding rocks (z^*). In the first equation, z^* is expressed as the difference between the time-integrated fluid flux within the rocks surrounding the shear zone $[(\omega\phi)_1]$ and the time-integrated fluid flux along the shear zone $[(\omega\phi)_2]$:

$$z^* = [(\omega\phi)_2 - (\omega\phi)_1]t \quad (2)$$

where ω is fluid velocity and ϕ is porosity. In the second equation, z^* is expressed as the difference between the X_{CO_2} of the fluid buffered by the reaction ($X_{\text{CO}_2,1}$) and the X_{CO_2} of fluid within the shear zone ($X_{\text{CO}_2,2}$) divided by the slope of the reaction curve on the P - T (or depth, z) vs X_{CO_2} diagram ($\partial X_{\text{CO}_2}/\partial z$ from Fig. 16b):

$$z^* = \frac{X_{\text{CO}_2,2} - X_{\text{CO}_2,1}}{(\partial X_{\text{CO}_2}/\partial z)}. \quad (3)$$

Combining equation (2) and (3) gives

$$(\omega\phi)_2 - (\omega\phi)_1 = \frac{X_{\text{CO}_2,2} - X_{\text{CO}_2,1}}{t(\partial X_{\text{CO}_2}/\partial z)}. \quad (4)$$

Combining equations (1) and (4) (i.e. substituting for $X_{\text{CO}_2,1}$) gives

$$(\omega\phi)_2 - (\omega\phi)_1 = \frac{X_{\text{CO}_2,2}}{t(\partial X_{\text{CO}_2}/\partial z)} \left[1 - \text{erfc} \left(\frac{x^*}{2\sqrt{D\phi\tau t}} \right) \right]. \quad (5)$$

Solving this equation with $X_{\text{CO}_2,2} = 0.0001$ and $X_{\text{CO}_2}/\partial z = 10^{-8} \text{ m}^{-1}$, estimated from Fig. 16b, $x^* = 1 \text{ m}$, estimated from Fig. 4, $(\omega\phi)_1 = 10^{-10.2 \pm 0.4} \text{ m}^3 \text{ m}^{-2} \text{ s}^{-1}$, $\phi = 10^{-2.6 \pm 0.2}$, $\tau = 0.68 \pm 0.03$ and $t = 10^{3.6 \pm 0.1}$ years from Skelton (2011) and $D = 10^{-8} \text{ m}^2 \text{ s}^{-1}$ from Wark & Watson (2003), we calculate that the fluid flux along the shear zone, $(\omega\phi)_2 = 10^{-7.5 \pm 0.3} \text{ m}^3 \text{ m}^{-2} \text{ s}^{-1}$. This fluid flux is 100–2000 times larger than the fluid flux within the surrounding rocks. The fluid flux we calculated for the shear zone equates to a fluid flux of $0.5\text{--}1.6 \text{ m}^3 \text{ m}^{-2} \text{ a}^{-1}$. This is faster than the value of $0.0035\text{--}0.35 \text{ m}^3 \text{ m}^{-2} \text{ a}^{-1}$ calculated by Dipple & Ferry (1992). This difference arises because Dipple & Ferry (1992) assumed a longer timescale than was assumed in our study. Recalculating their fluid flux for the shorter timescale assumed in our study gives a fluid flux of $4.4\text{--}7.0 \text{ m}^3 \text{ m}^{-2} \text{ a}^{-1}$. This is much closer to our estimated fluid flux. For laminar flow and using the above

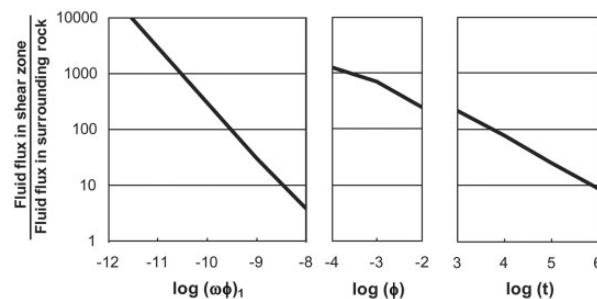


Fig. 19. Illustration of the change in fluid flux along the shear zone relative to plausible ranges of fluid flux in the surrounding rocks ($(\omega\phi)_1$, porosity ϕ and time t).

estimates of ϕ and τ from Skelton (2011), fluid viscosity, $\mu = 0.15 \text{ g cm}^{-1} \text{ s}^{-1}$ (from Dudziak & Franck, 1966), rock density $\rho_{\text{rock}} = 2.6\text{--}2.7 \text{ g cm}^{-3}$, fluid density $\rho_{\text{fluid}} = 1.0 \text{ g cm}^{-3}$ and channel width $d = \phi l/2$, where l = grain diameter (from Ferry & Dipple, 1991), we calculate a fluid flux of $0.3\text{--}1.2 \text{ m}^3 \text{ m}^{-2} \text{ a}^{-1}$ from the equation (Walther & Orville, 1982)

$$\omega = \frac{d^2}{12\mu} (\rho_{\text{rock}} - \rho_{\text{fluid}})g. \quad (6)$$

This is again similar to that which we estimated for the shear zone.

It is perhaps more useful to consider a range of input values to this calculation because many parameters are poorly constrained. Figure 19 shows how much faster fluid flow is calculated to be along the shear zone for plausible ranges of $(\omega\phi)_1$, ϕ and t . For $(\omega\phi)_1$ ranging from 10^{-8} to $10^{-12} \text{ m}^3 \text{ m}^{-2} \text{ s}^{-1}$, the fluid flux along the shear zone ranges from 4 to 30 000 times larger than the fluid flux within the surrounding rocks. For ϕ ranging from 10^{-2} to 10^{-4} (Connolly, 1997) the fluid flux along the shear zone ranges from 240 to 1200 times larger than the fluid flux within the surrounding rocks. For t ranging from 10^3 to 10^6 years, the fluid flux along the shear zone ranges from 210 to 9 times larger than the fluid flux within the surrounding rocks.

It is important to note that these estimated values are subject to a number of assumptions; this part of our study has therefore been included for illustrative purposes only and, at best, all we can provide is an order-of-magnitude estimate of the fluid flux along the shear zone. For example, our calculation assumes that the X_{CO_2} of fluid along the shear zone was elevated according to the mechanism shown in Fig. 18. If X_{CO_2} along the shear zone was externally controlled, our calculation is no longer valid. Also, our calculation assumes that it is valid to use values for fluid flux, porosity and time from Skelton (2011). In favour of this assumption being valid, we note that the Skelton (2011) study was conducted at near-identical P - T conditions. Finally, our estimates of $X_{\text{CO}_2,2}$ and $\partial X_{\text{CO}_2}/\partial z$

are based on a P – T vs X_{CO_2} pseudosection that was constructed for an oversimplified chemical system. However, because X_{CO_2} and $\partial X_{\text{CO}_2}/\partial z$ co-vary (because of the convexity of the T – X_{CO_2} curve) and because X_{CO_2} is divided by $\partial X_{\text{CO}_2}/\partial z$ in equation (5), we expect that this error will be small.

CONCLUSIONS

Based on petrological and geochemical data, we conclude that a carbonated blueschist-facies assemblage was preserved from greenschist-facies hydration alongside a shear zone on SE Syros in the Cyclades of southern Greece because of (1) metasomatic addition of SiO_2 and Na_2O and (2) elevated X_{CO_2} . Based on thermodynamic modeling, we propose a model whereby X_{CO_2} remains elevated because of a fast-flowing CO_2 -bearing fluid along the shear zone. Inferred metamorphic CO_2 fluxes are significantly higher than within the surrounding rocks. A simple mass-balance calculation reveals that the fluid flux along the shear zone required to cause the observed preservation of blueschist-facies minerals was 100–2000 times greater than the fluid flux in the surrounding rocks. We note that the proposed mechanism can be used to explain only local preservation of a carbonate-bearing blueschist-facies assemblage.

ACKNOWLEDGEMENTS

The authors would like to thank J. Majka, H. Harryson, R. Jacobsson and D. Zetterberg for their contribution during sample preparation and analyses. J. Ferry, J.C. Schumacher and an anonymous reviewer are thanked for constructive reviews and helpful comments. The authors also would like to thank J. Herman for careful and thoughtful editorial handling of this study.

FUNDING

This work was supported financially by an EU Initial Training Network Delta-Min (Mechanisms of Mineral Replacement Reactions) grant and was carried out within the framework of the Navarino Environmental Observatory (NEO), Messinia, Greece, a co-operation between Stockholm University, the Academy of Athens and TEMES S.A. The XRF analyses were performed at the XRF Facility of the Department of Geological Sciences, Stockholm University, which is partially supported by the Knut & Alice Wallenberg Foundation.

REFERENCES

- Ague, J. J. (2000). Release of CO_2 from carbonate rocks during regional metamorphism of lithologically heterogeneous crust. *Geology* **28**, 1123–1126.
- Ague, J. J. (2003a). Fluid flow in the deep crust. *Treatise on Geochemistry* **3**, 195–228.
- Ague, J. J. (2003b). Fluid infiltration and transport of major, minor, and trace elements during regional metamorphism of carbonate rocks, Wepawaug Schist, Connecticut, USA. *American Journal of Science* **303**, 753–816.
- Ague, J. J. (2007). Models of permeability contrasts in subduction zone mélange: Implications for gradients in fluid fluxes, Syros and Tinos Islands, Greece. *Chemical Geology* **239**, 217–227.
- Ague, J. J. (2011). Extreme channelization of fluid and the problem of element mobility during Barrovian metamorphism. *American Mineralogist* **96**, 333–352.
- Ague, J. J. & Nicolescu, S. (2014). Carbon dioxide released from subduction zones by fluid-mediated reactions. *Nature Geoscience* **7**, 355–360.
- Ague, J. J. & van Haren, J. L. M. (1996). Assessing metasomatic mass and volume changes using the bootstrap, with application to deep-crustal hydrothermal alteration of marble. *Economic Geology* **91**, 1169–1182.
- Altherr, R., Schliestedt, M., Okrusch, M., Seidel, E., Kreuzer, H., Harre, W., Lenz, H., Wendt, I. & Wagner, G. A. (1979). Geochronology of high pressure rocks on Sifnos (Cyclades, Greece). *Contributions to Mineralogy and Petrology* **70**, 245–255.
- Altherr, R., Kreuzer, H., Wendt, L., Lenz, H., Wagner, G. H., Keller, J., Harre, W. & Höhndorf, A. (1982). A late Oligocene/early Miocene high temperature belt in the Attic–Cycladic crystalline complex (SE Pelagonian, Greece). *Geologisches Jahrbuch* **23**, 97–164.
- Aubouin, J. & Dercourt, J. (1965). Sur la géologie de l'Égée: regard sur la Crète (Grèce). *Bulletin de la Société Géologique de France* **7**, 787–821.
- Avigad, D. (1993). Tectonic juxtaposition of blueschists and greenschists in Sifnos island (Aegean Sea)—implications for the structure of the Cycladic blueschist belt. *Journal of Structural Geology* **15**, 1459–1469.
- Avigad, D. & Garfunkel, Z. (1989). Low angle faults underneath and above a blueschist belt—Tinos Island, Cyclades, Greece. *Terra Nova* **1**, 182–187.
- Avigad, D. & Garfunkel, Z. (1991). Uplift and exhumation of high-pressure metamorphic terranes: the example of the Cyclades blueschist belt (Aegean Sea). *Tectonophysics* **188**, 357–372.
- Avigad, D., Matthews, A., Evans, B. W. & Garfunkel, Z. (1992). Cooling during the exhumation of a blueschist terrane: Sifnos (Cyclades, Greece). *European Journal of Mineralogy* **4**, 619–634.
- Avigad, D., Garfunkel, Z., Jolivet, L. & Azanon, J. M. (1997). Back arc extension and denudation of Mediterranean eclogites. *Tectonics* **16**, 924–941.
- Barnicoat, A. C. & Cartwright, I. (1995). Focused fluid flow during subduction: oxygen isotope data from high-pressure ophiolites of the western Alps. *Earth and Planetary Science Letters* **132**, 53–61.
- Barr, H. (1990). Preliminary fluid inclusion studies in high-grade blueschist terrain, Syros, Greece. *Mineralogical Magazine* **54**, 159–168.
- Barrientos, X. & Selverstone, J. (1993). Infiltration vs thermal overprinting of epidote blueschists, Ile de Groix, France. *Geology* **21**, 69–72.
- Baziotis, I., Proyer, A. & Mposkos, E. (2008). High-pressure/low-temperature metamorphism of basalts in Lavrion (Greece): implications for the preservation of peak metamorphic assemblages in blueschists and greenschists. *European Journal of Mineralogy* **21**, 133–148.
- Beach, A. & Tarney, J. (1978). Major and trace element patterns established during retrogressive metamorphism of granulite-facies gneisses, NW Scotland. *Precambrian Research* **7**, 325–348.
- Beinlich, A., Klemd, R., John, T. & Gao, J. (2010). Trace-element mobilization during Ca-metasomatism along a major fluid conduit:

- Eclogitization of blueschist as a consequence of fluid–rock interaction. *Geochimica et Cosmochimica Acta* **74**, 1892–1922.
- Bickle, M. J. & Baker, J. (1990). Advective–diffusive transport of isotopic fronts: an example from Naxos, Greece. *Earth and Planetary Science Letters* **97**, 78–93.
- Bickle, M. J. & McKenzie, D. (1987). The transport of heat and matter by fluids during metamorphism. *Contributions to Mineralogy and Petrology* **95**, 384–392.
- Brady, J. B. (1988). The role of volatiles in the thermal history of metamorphic terranes. *Journal of Petrology* **29**, 1187–1213.
- Breeding, C. M., Ague, J. J., Bröcker, M. & Bolton, E. W. (2003). Blueschist preservation in a retrograded, high-pressure, low-temperature metamorphic terrane, Tinos, Greece: Implications for fluid flow paths in subduction zones. *Geochemistry, Geophysics, Geosystems* **4**, 1–11.
- Breeding, C. M., Ague, J. J. & Bröcker, M. (2004). Fluid–metasedimentary rock interactions and the chemical composition of arc magmas. *Geology* **32**, 1041–1044.
- Bröcker, M. (1990). Blueschist-to-greenschist transition in metabasites from Tinos Island (Cyclades, Greece): Compositional control or fluid infiltration. *Lithos* **25**, 25–39.
- Bröcker, M. & Enders, M. (2001). Unusual bulk-rock composition in eclogite-facies rocks from Syros and Tinos (Cyclades, Greece): implications for U–Pb zircon geochronology. *Chemical Geology* **175**, 581–603.
- Bröcker, M. & Franz, L. (1998). Rb–Sr isotope studies on Tinos Island (Cyclades, Greece): additional time constraints for metamorphism, extent of infiltration-controlled overprinting and deformational activity. *Geological Magazine* **135**, 369–382.
- Bröcker, M., Kreuzer, H., Matthews, A. & Okrusch, M. (1993). ⁴⁰Ar/³⁹Ar and oxygen isotope studies of polymetamorphism from Tinos Island, Cycladic blueschist belt, Greece. *Journal of Metamorphic Geology* **11**, 223–240.
- Bröcker, M., Bieling, D., Hacker, B. & Gans, P. (2004). High-Si phengites record the time of greenschist-facies overprinting: implications for the models suggesting mega-detachments in the Aegean Sea. *Journal of Metamorphic Geology* **22**, 427–442.
- Brovarone, A. V., Groppo, C., Hetényi, G., Compagnoni, R. & Malavieille, J. (2011). Coexistence of lawsonite-bearing eclogite and blueschist: phase equilibria modeling of Alpine Corsica metabasalts and petrological evolution of subducting slabs. *Journal of Metamorphic Geology* **29**, 583–600.
- Connolly, J. A. D. (1990). Multivariable phase-diagrams—an algorithm based on generalized thermodynamics. *American Journal of Science* **290**, 666–718.
- Connolly, J. A. D. (1997). Delvolatilization-generated fluid pressure and deformation-propagated fluid flow during prograde regional metamorphism. *Journal of Geophysical Research* **102**, 18149–18173.
- Connolly, J. A. D. (2005). Computation of phase equilibria by linear programming: A tool for geodynamic modeling and its application to subduction zone decarbonation. *Earth and Planetary Science Letters* **236**, 524–541.
- Connolly, J. A. D. (2009). The geodynamic equation of state: What and how. *Geochemistry, Geophysics, Geosystems* **10**, doi:10.1029/2009GC00254.
- Dale, J., Powell, R., White, R. W., Elmer, F. L. & Holland, T. J. B. (2005). A thermodynamic model for Ca–Na clinoamphiboles in Na₂O–CaO–FeO–MgO–Al₂O₃–SiO₂–H₂O–O for petrological calculations. *Journal of Metamorphic Geology* **23**, 771–791.
- Diener, J. F. A. & Powell, R. (2010). Influence of ferric iron on the stability of mineral assemblages. *Journal of Metamorphic Geology* **28**, 599–613.
- Dipple, G. M. & Ferry, J. M. (1992). Metasomatism and fluid flow in ductile fault zones. *Contributions to Mineralogy and Petrology* **112**, 149–164.
- Dixon, J. E. & Ridley, J. (1987). Syros. In: Helgeson, H. C. (ed.) *Chemical Transport in Metasomatic Processes*. Reidel, pp. 489–501.
- Drury, S. A. (1974). Chemical changes during retrogressive metamorphism of Lewisian granulite facies rocks from Coll and Tiree. *Scottish Journal of Geology* **10**, 237–256.
- Dudziak, K. H. & Franck, E. U. (1966). Messungen der Viskosität des Wassers bis 560°C und 3500 bar. *Berichte der Bunsengesellschaft für Physikalische Chemie* **70**, 1120–1128.
- Dürr, S., Altherr, R., Okrusch, M. & Seidel, E. (1978). The median Aegean Belt; stratigraphy, structure metamorphism. In: Closs, H., Roeder, D. & Schmidt, K. (eds) *Alps, Apennines, Hellenides*. Schweizerbart'sche, pp. 455–477.
- Ernst, W. G. (2006). Preservation/exhumation of ultrahigh-pressure subduction complexes. *Lithos* **92**, 321–335.
- Evans, B. W. (1990). Phase relations of epidote-blueschists. *Lithos* **25**, 3–23.
- Famin, V., Philippot, P., Jolivet, L. & Agard, P. (2004). Evolution of hydrothermal regime along a crustal shear zone, Tinos Island, Greece. *Tectonics* **23**, doi:10.1029/2003TC001509.
- Ferry, J. M. & Dipple, G. M. (1991). Fluid flow, mineral reactions and metasomatism. *Geology* **19**, 211–214.
- Franz, G. & Liebscher, A. (2004). Physical and chemical properties of the epidote minerals—An introduction. In: Liebscher, A. & Franz, G. (eds) *Epidotes. Mineralogical Society of America and Geochemical Society, Reviews in Mineralogy and Geochemistry* **56**, 1–82.
- Fyfe, W. S., Price, N. J. & Thompson, A. B. (1978). *Fluids in Earth's Crust*. Elsevier, 383 p.
- Ganor, J., Matthews, A. & Schliestedt, M. (1994). Post-metamorphic low $\delta^{13}\text{C}$ veins in the Cycladic metamorphic complex (Greece) and their implications for modeling fluid infiltration processes using carbon isotope compositions. *European Journal of Mineralogy* **6**, 365–379.
- Ganor, J., Matthews, A., Schliestedt, M. & Garfunkel, Z. (1996). Oxygen isotope heterogeneities of metamorphic rocks: an original tectonostratigraphic signature, or an imprint of exotic fluids? A case study of Sifnos and Tinos Islands (Greece). *European Journal of Mineralogy* **8**, 719–731.
- Gao, J. & Klemd, R. (2001). Primary fluids entrapped at the blueschist to eclogite transition: evidence from the Tianshan metasubduction complexes in north-western China. *Contributions to Mineralogy and Petrology* **142**, 1–14.
- Getty, S. & Selverstone, J. (1994). Stable isotopic and trace element evidence for restricted fluid migration in 2 GPa eclogites. *Journal of Metamorphic Geology* **12**, 747–760.
- Grant, J. A. (1986). The Isocon diagram—A simple solution to Gresens' equation for metasomatic alteration. *Economic Geology* **81**, 1976–1982.
- Holland, T. & Powell, R. (1998). An internally consistent thermodynamic data set for phases of petrological interest. *Journal of Metamorphic Geology* **16**, 309–343.
- Holland, T. J. B. & Powell, R. (2003). Activity–composition relations for phases in petrological calculations: an asymmetric multicomponent formulation. *Contributions to Mineralogy and Petrology* **145**, 492–501.
- Holland, T. J. B., Baker, J. & Powell, R. (1998). Mixing properties and activity–composition relationships of chlorites in the system MgO–FeO–Al₂O₃–SiO₂–H₂O. *European Journal of Mineralogy* **10**, 395–406.
- Jacobshagen, V., Duerr, S., Kockel, F., Kopp, K. O., Kowalczyk, G., Berckhemer, H. & Buettner, D. (1978). Structure and geodynamic

- evolution of the Aegean region. In: Close, H., Roeder, D. & Schmidt, K. (eds) *Alps, Apennines, Hellenides. Inter-Union Commission on Geodynamics Scientific Report* **38**, 537–564.
- Jolivet, L. & Brun, J.-P. (2010). Cenozoic geodynamic evolution of the Aegean. *International Journal of Earth Sciences* **99**, 109–138.
- Jolivet, L., Faccenna, C., Goffé, B., Burow, E. & Agard, P. (2003). Subduction tectonics and exhumation of high-pressure metamorphic rocks in the Mediterranean orogens. *American Journal of Science* **303**, 353–409.
- Jolivet, L., Faccenna, C., Huet, B. *et al.* (2013). Aegean tectonics: Strain localisation, slab tearing and trench retreat. *Tectonophysics* **597–598**, 1–33.
- Keiter, M., Piepjohn, K., Ballhaus, C., Bode, M. & Lagos, M. (2004). Structural development of high-pressure metamorphic rocks on Syros island (Cyclades, Greece). *Journal of Structural Geology* **26**, 1433–1445.
- Keiter, M., Ballhaus, C. & Tomaschek, F. (2011). *A new geological map of the Island of Syros (Aegean Sea, Greece): Implications for lithostratigraphy and structural history of the Cycladic Blueschist Unit. Geological Society of America, Special Papers* **481**, 43 p.
- Kerrick, D. M. & Caldeira, K. (1998). Metamorphic CO₂ degassing from orogenic belts. *Chemical Geology* **145**, 213–232.
- Lagos, M., Scherer, E. E., Tomaschek, F., Muenker, C., Keiter, M., Berndt, J. & Ballhaus, C. (2007). High precision Lu–Hf geochronology of Eocene eclogite-facies rocks from Syros, Cyclades, Greece. *Chemical Geology* **243**, 16–35.
- Leake, B. E., Woolley, A. R., Arps, C. E. S. *et al.* (1997). Nomenclature of amphiboles: Report of the Subcommittee on Amphiboles of the International Mineralogical Association, Commission on New Minerals and Mineral Names. *American Mineralogist* **82**, 1019–1037.
- Maluski, H., Bonneau, M. & Kienast, J. R. (1987). Dating the metamorphic events in the Cycladic area: ³⁹Ar/⁴⁰Ar data from metamorphic rocks of the island of Syros (Greece). *Bulletin de la Société Géologique de France* **8**, 833–842.
- Matthews, A. & Schliestedt, M. (1984). Evolution of the blueschist and greenschist facies rocks of Sifnos, Cyclades, Greece. *Contributions to Mineralogy and Petrology* **88**, 150–163.
- Mikuchi, E. J. & Ridley, J. R. (1993). The hydrothermal fluid of Archean lode gold deposits at different metamorphic grades: compositional constraints from ore and wall rock alteration assemblages. *Mineralium Deposita* **28**, 469–481.
- Miller, D. P., Marschall, H. R. & Schumacher, J. C. (2009). Metasomatic formation and petrology of blueschist-facies hybrid rocks from Syros (Greece): Implications for reactions at the slab–mantle interface. *Lithos* **107**, 53–67.
- Okrusch, M. & Bröcker, M. (1990). Eclogite facies rocks in the Cycladic blueschist belt, Greece: A review. *European Journal of Mineralogy* **2**, 451–478.
- Owen, C. (1989). Magmatic differentiation and alteration in isofacial greenschists and blueschists, Shuksan Suite, Washington: Statistical analysis of major-element variation. *Journal of Petrology* **30**, 739–761.
- Parra, T., Vidal, O. & Jolivet, L. (2002). Relation between the intensity of deformation and retrogression in blueschist metapelites of Tinos Island (Greece) evidenced by chlorite–mica local equilibria. *Lithos* **63**, 41–66.
- Patzak, M., Okrusch, M. & Kreuzer, H. (1994). The Akrotiri Unit on the island of Tinos, Cyclades, Greece: Witness to a lost terrane of Late Cretaceous age. *Neues Jahrbuch für Mineralogie, Abhandlungen* **194**, 211–252.
- Philippon, M., Brun, J.-P. & Gueydan, F. (2011). Tectonics of the Syros blueschists (Cyclades, Greece): From subduction to Aegean extension. *Tectonics* **30**, doi:10.1029/2010TC002810.
- Philippot, P. & Selverstone, J. (1991). Trace-element-rich brines in eclogitic veins: implications for fluid composition and transport during subduction. *Contributions to Mineralogy and Petrology* **106**, 417–430.
- Putlitz, B., Matthews, A. & Valley, J. W. (2000). Oxygen and hydrogen isotope study of high pressure metagabbros and metabasalts (Cyclades, Greece): implications for the subduction of oceanic crust. *Contributions to Mineralogy and Petrology* **138**, 114–126.
- Putlitz, B., Cosca, M. A. & Schumacher, J. C. (2005). Prograde mica ³⁹Ar/⁴⁰Ar growth ages recorded in high pressure rocks (Syros, Cyclades, Greece). *Chemical Geology* **214**, 79–98.
- Reinecke, T., Altherr, R., Hartung, B., Hatzipanagiotou, K., Kreuzer, H., Harre, W., Klein, H., Keller, J., Geenen, E. & Boger, H. (1982). Remnants of a Late Cretaceous high temperature belt on the island of Anafi (Cyclades, Greece). *Neues Jahrbuch für Mineralogie, Abhandlungen* **145**, 157–182.
- Ring, U. & Layer, P. W. (2003). High-pressure metamorphism in the Aegean, eastern Mediterranean: underplating and exhumation from the Late Cretaceous until the Miocene to Recent above the retreating Hellenic subduction zone. *Tectonics* **22**, doi:10.1029/2001TC001350.
- Ring, U., Thomson, S. T. & Bröcker, M. (2003). Fast extension but little exhumation: the Vari detachment in the Cyclades, Greece. *Geological Magazine* **140**, 245–252.
- Ring, U., Will, T., Glodny, J., Kumerics, C., Gessner, K., Thomson, S., Gungor, T., Monie, P., Okrusch, M. & Druppel, K. (2007). Early exhumation of high-pressure rocks in extrusion wedges: Cycladic blueschist unit in the eastern Aegean, Greece, and Turkey. *Tectonics* **26**, doi:10.1029/2005TC001872.
- Ring, U., Glodny, J., Will, T. & Thomson, S. (2010). The Hellenic subduction system: high-pressure metamorphism, exhumation, normal faulting, and large-scale extension. *Annual Review of Earth and Planetary Sciences* **38**, 45–76.
- Robert, F., Boullier, A. M. & Firdaous, K. (1995). Gold–quartz veins in metamorphic terranes and their bearing on the role of fluids in faulting. *Journal of Geophysical Research: Solid Earth* **100**, 12861–12879.
- Rosenbaum, G., Avigad, D. & Sanchez-Gomez, M. (2002). Coaxial flattening at deep levels of orogenic belts: evidence from blueschists and eclogites on Syros and Sifnos (Cyclades, Greece). *Journal of Structural Geology* **24**, 1451–1462.
- Schliestedt, M. (1986). Eclogite–blueschist relationships as evidenced by mineral equilibria in the high-pressure metabasic rocks of Sifnos (Cycladic Islands), Greece. *Journal of Petrology* **27**, 1437–1459.
- Schliestedt, M. & Matthews, A. (1987). Transformation of blueschist to greenschist facies rocks as a consequence of fluid infiltration, Sifnos (Cyclades), Greece. *Contributions to Mineralogy and Petrology* **97**, 237–250.
- Schumacher, J. C., Brady, J. B. & Cheney, J. T. (2008a). Metamorphic style and development of the blueschist- to eclogite-facies rocks, Cyclades, Greece. *Earth and Environmental Science* **2**, 1–6.
- Schumacher, J. C., Brady, J. B., Cheney, J. T. & Tønnsen, R. R. (2008b). Glaucophane-bearing marbles on Syros, Greece. *Journal of Petrology* **49**, 1667–1686.
- Selverstone, J., Franz, G., Thomas, S. & Getty, S. (1992). Fluid variability in 2 GPa eclogites as an indicator of fluid behaviour during subduction. *Contributions to Mineralogy and Petrology* **112**, 341–357.
- Skelton, A. D. L. (2011). Flux rates for water and carbon during greenschist facies metamorphism. *Geology* **39**, 43–46.
- Skelton, A. D. L., Graham, C. M. & Bickle, M. J. (1995). Lithological and structural controls on regional 3-D fluid flow patterns during

- greenschist facies metamorphism of the Dalradian of the SW Scottish Highlands. *Journal of Petrology* **36**, 563–586.
- Soukis, K. & Stöckli, D. F. (2013). Structural and thermochronometric evidence for multi-stage exhumation of southern Syros, Cycladic islands, Greece. *Tectonophysics* **595–596**, 148–164.
- Spear, F. S. (1993). Crystal chemistry of rock-forming minerals. In: Spear, F. S. (ed.) *Metamorphic Phase Equilibria and Pressure–Temperature–Time Paths*. Mineralogical Society of America, pp. 73–105.
- Tischendorf, G., Rieder, M., Förster, H.-J., Gottesmann, B. & Guidotti, C.V. (2004). A new graphical presentation and subdivision of potassium micas. *Mineralogical Magazine* **68**, 649–667.
- Tomaschek, F., Baumann, A., Villa, I. M., Kennedy, A. & Ballhaus, C. (2000). Geochronological constraints on a Cretaceous metamorphic event from the Vari Unit (Syros, Cyclades, Greece). *Beihfte zum European Journal of Mineralogy* **12**, 214.
- Tomaschek, F., Kennedy, A., Villa, I., Lagos, M. & Ballhaus, C. (2003). Zircons from Syros, Cyclades, Greece—Crystallization and mobilization during high pressure metamorphism. *Journal of Petrology* **44**, 1977–2002.
- Trotet, F., Jolivet, L. & Vidal, O. (2001a). Exhumation of Syros and Sifnos metamorphic rocks (Cyclades, Greece). New constraints on the *P–T* paths. *European Journal of Mineralogy* **13**, 901–920.
- Trotet, F., Jolivet, L. & Vidal, O. (2001b). Tectonometamorphic evolution of Syros and Sifnos islands. *Tectonophysics* **338**, 179–206.
- Van der Plas, L. & Tobi, A. C. (1965). A chart for judging the reliability of point counting results. *American Journal of Science* **263**, 87–90.
- Wallmann, K. (2001a). The geological water cycle and Cenozoic evolution of marine $\delta^{18}\text{O}$ values. *Geochimica et Cosmochimica Acta* **65**, 2469–2485.
- Wallmann, K. (2001b). Controls on the Cretaceous and Cenozoic evolution of seawater composition, atmospheric CO_2 and climate. *Geochimica et Cosmochimica Acta* **65**, 3005–3025.
- Walther, J. V. & Orville, P. M. (1982). Volatile production and transport in regional metamorphism. *Contributions to Mineralogy and Petrology* **79**, 252–257.
- Wark, D. A. & Watson, E. B. (2003). Interdiffusion of H_2O and CO_2 in metamorphic fluids at ~ 490 to 690°C and 1 GPa. *Geochimica et Cosmochimica Acta* **68**, 2693–2698.
- Wijbrans, J. R., Schliestedt, M. & York, D. (1990). Single grain argon laser probe dating of phengites from the blueschist to greenschist transition on Sifnos (Cyclades, Greece). *Contributions to Mineralogy and Petrology* **104**, 582–593.
- Zack, T. & John, T. (2007). An evaluation of reactive fluid flow and trace element mobility in subducting slabs. *Chemical Geology* **239**, 199–216.
- Zeffren, S., Avigad, D., Heimann, A. & Gvirtzman, Z. (2005). Age resetting of hanging wall rocks above a Tertiary low-angle detachment, Tinos island, Aegean Sea. *Tectonophysics* **400**, 1–25.